

Reexamining the potential to classify lava flows from the fractality of their margins

Ethan Immanuel Schaefer^{1,1}, Christopher W. Hamilton^{2,2}, Catherine Neish^{1,1}, Michael Sori³, Ali Bramson³, and Sky Beard⁴

¹University of Western Ontario

²University of Arizona

³Purdue University

⁴Macau University of Science and Technology

November 30, 2022

Abstract

Can fractal analysis of a lava flow’s margin enable classification of the lava’s morphologic type (e.g., pāhoehoe)? Such classifications would provide insights into the rheology and dynamics of the flow when it was emplaced. The potential to classify lava flows from remotely-sensed data would particularly benefit the analysis of flows that are inaccessible, including flows on other planetary bodies. The technique’s current interpretive framework depends on three assumptions: (1) measured margin fractality is scale-invariant; (2) morphologic types can be uniquely distinguished based on measured margin fractality; and (3) modification of margin fractality by topography, including substrate slope and confinement, would be minimal or independently recognizable. We critically evaluate these assumptions at meter scales (1–10 m) using 15 field-collected flow margin intervals from a wide variety of morphologic types in Hawai’i, Iceland, and Idaho. Among the 12 margin intervals that satisfy the current framework’s suitability criteria (e.g., geomorphic freshness, shallowly-sloped substrates), we show that 5 exhibit notably scale-dependent fractality and all 5 from lava types other than ‘a‘ā or pāhoehoe would be classified as one or both of those types at some scales. Additionally, an ‘a‘ā flow on a 15° slope (Mauna Ulu, Hawai’i) and a spiny pāhoehoe flow confined by a stream bank (Holuhraun, Iceland) exhibit significantly depressed fractalities but lack diagnostic signatures for these modifications. We therefore conclude that all three assumptions of the current framework are invalid at meter scales and propose a new framework to leverage the potential of the underlying fractal technique while acknowledging these complexities.

1
2
3
4
5
6
7
8
9
10
11
12
13
14
15
16
17
18
19
20
21
22

Reexamining the potential to classify lava flows from the fractality of their margins

E. I. Schaefer^{1,2}, C. W. Hamilton³, C. D. Neish^{1,2}, M. M. Sori⁴, A. M. Bramson⁴, and S. P. Beard⁵

¹ Department of Earth Sciences, University of Western Ontario, 1151 Richmond Street N., London, Ontario, N6A 5B7 Canada

² Institute for Earth and Space Exploration, University of Western Ontario, 1151 Richmond Street N., London, Ontario, N6A 5B7 Canada

³ Lunar and Planetary Laboratory, University of Arizona, 1629 E. University Blvd., Tucson, Arizona, 85721 USA

⁴ Department of Earth, Atmospheric, and Planetary Sciences, Purdue University, 550 Stadium Mall Dr., West Lafayette, IN 47907 USA

⁵ State Key Laboratory in Lunar and Planetary Science, Macau University of Science and Technology, Avenida Wai Long, Taipa, 999078 Macau

Corresponding author: Ethan I. Schaefer (ethan.i.schaefer@gmail.com)

Key Points:

- The fractality of lava flow margins is highly diverse and shows varying scale dependence, even among flows of the same morphologic type.
- Topographic confinement and substrate slopes can modify the fractality of a lava flow's margin without imparting a diagnostic signature.
- We incorporate these complexities in a new framework for interpreting lava flow types from the meter-scale fractality of flow margins.

23 Abstract

24 Can fractal analysis of a lava flow's margin enable classification of the lava's
25 morphologic type (e.g., pāhoehoe)? Such classifications would provide insights into the rheology
26 and dynamics of the flow when it was emplaced. The potential to classify lava flows from
27 remotely-sensed data would particularly benefit the analysis of flows that are inaccessible,
28 including flows on other planetary bodies. The technique's current interpretive framework
29 depends on three assumptions: (1) measured margin fractality is scale-invariant; (2) morphologic
30 types can be uniquely distinguished based on measured margin fractality; and (3) modification of
31 margin fractality by topography, including substrate slope and confinement, would be minimal or
32 independently recognizable. We critically evaluate these assumptions at meter scales (1–10 m)
33 using 15 field-collected flow margin intervals from a wide variety of morphologic types in
34 Hawai'i, Iceland, and Idaho. Among the 12 margin intervals that satisfy the current framework's
35 suitability criteria (e.g., geomorphic freshness, shallowly-sloped substrates), we show that 5
36 exhibit notably scale-dependent fractality and all 5 from lava types other than 'a'ā or pāhoehoe
37 would be classified as one or both of those types at some scales. Additionally, an 'a'ā flow on a
38 15° slope (Mauna Ulu, Hawai'i) and a spiny pāhoehoe flow confined by a stream bank
39 (Holuhraun, Iceland) exhibit significantly depressed fractalities but lack diagnostic signatures for
40 these modifications. We therefore conclude that all three assumptions of the current framework
41 are invalid at meter scales and propose a new framework to leverage the potential of the
42 underlying fractal technique while acknowledging these complexities.

43 1 Introduction

44 Fractal analysis provides an elegant way to describe complex natural geometries such as
45 lava margins (Avnir et al., 1998; Mandelbrot, 1982). It may also hold substantial promise to
46 constrain the rheology, emplacement dynamics, and chemical composition of flows. Bruno et al.
47 (1992) and Gaonac'h et al. (1992) were the first to demonstrate that the geometries of lava flow
48 margins are empirically fractal. That is, the apparent length of these margins, when measured at
49 progressively coarser resolutions, approximately decreases by a power-law over some range of
50 scales. Because fractal geometries naturally arise from nonlinear processes, the fractal analysis of
51 lava margins was expected to provide direct insights into the fluid dynamics of lava flows (e.g.,
52 Bruno et al., 1992, 1994; Gaonac'h et al., 1992; Kilburn, 1996). Moreover, Bruno et al. (1992,
53 1994) and Gaonac'h et al. (1992) presented evidence that the empirical fractality of lava margins
54 might extend from decimeter to kilometer scales, and Bruno et al. (1992, 1994) demonstrated
55 that this fractality could help to discriminate between two morphologic lava types: 'a'ā and
56 pāhoehoe. Knowledge of a flow's morphologic type can, in turn, help to constrain the dynamics,
57 rheology, effusion rate, and crustal disruption history of the lava at the time of its emplacement
58 (e.g., Cashman et al., 1999; Hamilton, 2019; Peterson & Tilling, 1980; Rowland & Walker,
59 1990). In addition, Bruno et al. (1994) found that flows of intermediate to silicic composition had
60 measured lengths that departed from power-law scaling, at least at scales of hundreds of meters,
61 suggesting that fractal analysis of margin geometries could be used to distinguish mafic lavas
62 from those with more evolved compositions.

63 Any insights provided by margin fractal analysis would especially facilitate the
64 characterization of flows in remote areas. Although field observations of lava flows provide
65 better constraints (e.g., Harris et al., 2017; Keszthelyi, 2002; Self et al., 1996; Thordarson, 1995),
66 such ground-truthing is not always feasible. For that reason, researchers have used margin fractal

67 analysis to investigate submarine lava flows on Earth (Maeno et al., 2016; Mitchell et al., 2008;
68 Wroblewski et al., 2019) and flows of lava and impact melt on Mars, Venus, and Earth's moon
69 (Bray et al., 2018; Bruno et al., 1992, 1994; Bruno & Taylor, 1995; Wroblewski et al., 2019;
70 You et al., 1996). As examples, margin fractal analysis may provide constraints on lava type,
71 which in turn could be used to infer eruption style and possibly magma source depths (Wilson &
72 Head, 1994), and supplement radar-derived surface roughness analyses to help clarify the
73 emplacement history of vast volcanic deposits on Venus (Campbell & Campbell, 1992). On
74 Earth, margin fractal analysis may also facilitate the planning of field campaigns. Flow margins
75 could be mapped using remotely-sensed data, and fractal analysis of these margins could reveal
76 distinct populations or anomalous flows that merit further investigation in the field.

77 The prevailing classification framework for the fractal analysis of mafic lava margins,
78 due to Bruno et al. (1994), depends explicitly on three assumptions: (1) The measured fractality
79 of a margin interval does not critically depend on the scale range over which that fractality is
80 measured. (2) The measured margin fractalities of 'a'ā, pāhoehoe, and so-called transitional lava
81 types are each distinct. (3) The effects of topography, including sloped substrates and
82 confinement, typically render a margin empirically non-fractal rather than merely modulate its
83 empirical fractality. Where this framework is used to classify flows remotely, the results may
84 depend critically on these assumptions. We therefore test each of these assumptions at meter
85 scales (~1–10 m) using 15 field-collected margin intervals from a wide variety of morphologic
86 types in Hawai'i, Iceland, and Idaho (Figure 1).

87 We first review the relevant background information (section 2) that motivates us to test
88 the assumptions enumerated above. We then explain how we interpret and quantify fractality in
89 this study, including some methodological refinements to the fractal analysis of lava margins
90 (section 3). We present our results (section 4) and then discuss how these results affect the
91 interpretation of morphologic type from margin fractal analysis (section 5), including
92 presentation of a new interpretive framework (section 5.3). Finally, we summarize our principal
93 conclusions (section 6).

94 **2 Background**

95 2.1 Scale dependence

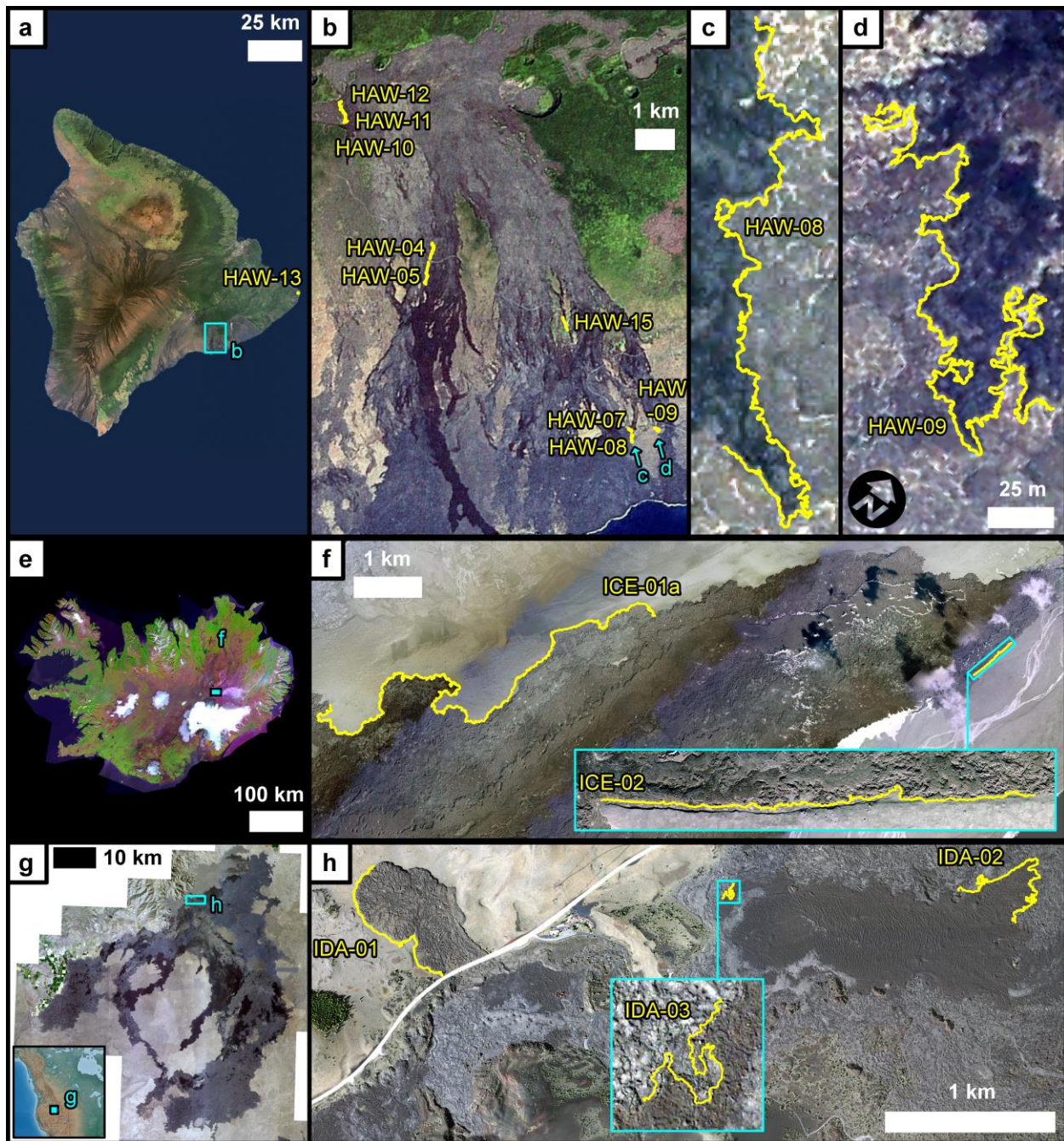
96 The effective fractal dimension D (section 3.2.2) quantifies the fractality of a geometry.
97 Because D depends on scaling behavior, each measurement of D must be made over a range of
98 scales. Based on this measurement characteristic, a D measured for a natural geometry has
99 traditionally been interpreted to be scale-invariant over the analyzed scale range, that is, to apply
100 consistently across the entire range of scales over which that D was calculated, unless scale
101 dependence is conspicuous. Although mathematical fractals that are self-similar (section 3.2.1)
102 do indeed have scale-invariant fractality, the default assumption of scale-invariant fractality for
103 natural geometries has been questioned by some (e.g., Avnir et al., 1998; Shenker, 1994). (For
104 further discussion, see section 3.2.1.)

105 In particular, the fractal analysis of topographic contours, including coastlines, provides a
106 cautionary parallel to the fractal analysis of lava margins. The D values of topographic contours
107 were long thought to be scale-invariant (Mandelbrot, 1967; Richardson, 1961), but later work
108 showed that these contours had distinctly different D values when measured over discrete scale
109 ranges (Mark & Aronson, 1984). Still later, Andrieu (1992, 1996b, 1996a) presented evidence

110 that coastlines' D values vary continuously with scale, including D values for the west coast of
111 Britain, which is the archetypal natural fractal (Mandelbrot, 1967; Richardson, 1961).

112 In the divider method (section 3.2.2) used by Bruno et al. (1994) and in the present study,
113 the analyzed scale range for each D is defined by a discrete set of scales. We call such a set a
114 "rod set", as each scale was traditionally measured using a different physical rod of that length.
115 The parameter r^* provides a single representative length value for a given rod set (section 3.2.4).
116 The lava margin fractal analyses of Bruno et al. (1994) included 27 field analyses, collectively
117 spanning scales of 0.125–16 m, and 17 photographic analyses, collectively spanning scales of
118 12–2400 m. Bruno et al. (1994) did not specify the rod set used in each D measurement, but they
119 did provide some generalities. In each field analysis, they used exactly one rod set (and therefore
120 calculated exactly one D) per margin interval. Moreover, each rod set used in field analysis was
121 selected from a collection of rods with lengths 0.125 m, 0.25 m, 0.5 m, 1 m, 2 m, 4 m, 8 m, and
122 16 m. Wherever possible, they specifically used a rod set of either 1–16 m or 0.5–16 m
123 (corresponding to representative scales of $r^* = 4$ m and $r^* = 2.83$ m, respectively). For shorter
124 margin intervals, they used rods as short as 0.125 m ($r^* \geq 0.5$ m). Their use of only one rod set
125 per field-analyzed margin interval and the preferential use of similar rod sets in field analyses
126 could potentially mask any scale-dependent fractality at meter scales (see also section 5.2.1),
127 which are the focus of the present study.

128



129

130 **Figure 1.** Locations of all 15 margin intervals (yellow lines) analyzed in the present study. (a)
 131 The island of Hawai‘i. (b) Study area in Hawai‘i Volcanoes National Park. (c)–(d): Magnified
 132 views of two margin intervals from (b). (e) Iceland. (f) Two margin intervals from the 2014–
 133 2015 Holuhraun flow field. (g) Study area and (h) margin intervals in Craters of the Moon
 134 National Monument and Preserve, Idaho, USA. Inset in (g) shows location in North America.
 135 Background of (a) and (b) is a Landsat 7 mosaic (15 m/pixel) created by Earthstar Geographics.
 136 Background of (c) and (d) is a QuickBird orthomosaic (0.6 m/pixel) from the Natural Resources
 137 Conservation Service of the United States Department of Agriculture. Background of (e) is a
 138 Landsat 8 mosaic (66 m/pixel) created by the National Land Survey of Iceland. Background of

139 (f) is a color orthoimage from Loftmyndir ehf. (0.5 m/pixel). Backgrounds of (g) and (h) are
 140 orthoimages (0.5 m/pixel) from the National Agriculture Imagery Program of the United States
 141 Department of Agriculture. North is up in all views except for (d) and the inset in (f).

142

143 In three cases, Bruno et al. (1994) also analyzed the same margin—albeit over different
 144 intervals—in paired field and photographic analyses. The measured disparities were similar to
 145 the single-rod-set along-length variabilities in D that they measured. They therefore interpreted
 146 D to be scale-invariant, but the limited scope of these paired analyses—three pāhoehoe margins,
 147 all from Hawai‘i, each analyzed with exactly two rod sets (one from the field and one from
 148 photographs)—may not be sufficient to characterize the frequency of scale-dependent fractality
 149 across morphologic types and geologic settings, especially at meter scales.

150 When exploring scale dependence, we primarily focus on meter scales (~ 1 – 10 m), though
 151 we also report results at coarser scales when possible. Meter scales are best supported by our
 152 data and were the primary focus of Bruno et al. (1994), whose study is the most extensive
 153 investigation of lava margin fractality to date. The scale dependence of empirical lava margin
 154 fractality is also least constrained at these scales, as described earlier in this section.
 155 Furthermore, meter scales are relevant in both terrestrial and planetary contexts. These scales are
 156 resolvable on Mars by the High Resolution Imaging Science Experiment (HiRISE) on board the
 157 *Mars Reconnaissance Orbiter*, which has a minimum pixel scale of 25 cm/pixel (McEwen et al.,
 158 2007), and on Earth’s moon by both the Narrow Angle Cameras on board the *Lunar*
 159 *Reconnaissance Orbiter*, which has a minimum pixel scale of 50 cm (Robinson et al., 2010), and
 160 the Orbiter High Resolution Camera on board *Chandrayaan-2*, which has a minimum pixel scale
 161 of 25 cm (Chowdhury et al., 2020).

162 2.2 Morphologic lava types

163 Morphologic lava types are commonly classified in a three-part system of ‘a‘ā, pāhoehoe,
 164 and block lava (Harris et al., 2017; Macdonald, 1953). ‘A‘ā and pāhoehoe are most commonly
 165 associated with mafic lava, whereas block lavas typically are more silicic (Finch, 1933). Other
 166 mafic lavas that are neither ‘a‘ā nor pāhoehoe are conventionally called “transitional” (see
 167 section 2.2.2). We direct the reader to Harris et al. (2017), Gregg (2017), and Hamilton (2019)
 168 for detailed descriptions of these lava types. Although lava types are traditionally distinguished
 169 by sub-meter surface morphology, they can also be identified from interior structure (e.g., Harris
 170 et al., 2017; Keszthelyi, 2002; Self et al., 1996; Thordarson, 1995). We include examples of ‘a‘ā,
 171 pāhoehoe, and transitional lavas in the present study, as well as one example of lava that may be
 172 intermediate between block lava and ‘a‘ā (Table 1).

173 2.2.1 ‘A‘ā and pāhoehoe

174 Whether basaltic lava freezes to form a crust of ‘a‘ā or pāhoehoe is determined by both
 175 the rheology and dynamics of the flow, with pāhoehoe favored by lower apparent viscosities and
 176 lower shear strain rates (Macdonald, 1953; Peterson & Tilling, 1980). These properties can be
 177 interpreted as lower yield strengths and lower rates of net crustal disruption, respectively
 178 (Cashman et al., 1999; Kilburn, 1990). A flow can also transition from pāhoehoe to ‘a‘ā (or,
 179 more rarely, from ‘a‘ā to pāhoehoe) as the apparent viscosity and/or shear strain rate change
 180 along the flow’s path (Hon et al., 2003; Lipman & Banks, 1987; Macdonald, 1953; Wolfe et al.,

181 1988). For example, steep substrates can increase local flow velocities and hence shear strain
 182 rate, such that pāhoehoe transitions to ‘a‘ā (e.g., Macdonald, 1953; Peterson & Tilling, 1980).

183 Bruno et al. (1994) primarily focused on margins of ‘a‘ā and pāhoehoe. We therefore
 184 include nine margin intervals of ‘a‘ā or pāhoehoe to facilitate comparison of our results to theirs.

185 2.2.2 Transitional lavas

186 The genetic interpretation of transitional lavas is more complicated than that of ‘a‘ā and
 187 pāhoehoe. Several workers have reported continuous and long-lived formation of transitional
 188 lavas at active flows (e.g., Lipman & Banks, 1987; Pedersen et al., 2017), whereas others have
 189 interpreted transitional lavas to form from episodic disruption of otherwise stable crusts
 190 (Hamilton, 2019; Keszthelyi et al., 2004). Further research is necessary to clarify the origins of
 191 and relationships between transitional types (cf. Cashman et al., 1999; Hon et al., 2003; Kilburn,
 192 1990; Peterson & Tilling, 1980; Soule & Cashman, 2005).

193 To reasonably classify lavas, one must consider transitional types in addition to the
 194 traditional ‘a‘ā and pāhoehoe end-members. For example, pāhoehoe and rubbly lava are the
 195 dominant types in Iceland (Thordarson & Höskuldsson, 2008). Rubbly and slabby lavas may also
 196 be important on Mars, based on the observation of similar morphologies in terrestrial and
 197 Martian flow fields at scales of tens of meters or more (Keszthelyi et al., 2000, 2004; Voigt &
 198 Hamilton, 2018). These observations motivate us to include transitional types in our analysis,
 199 especially as these types have not yet been a major focus of margin fractal analysis (cf. Bruno et
 200 al., 1994). Six of our margin intervals target one or more transitional types, and two of these
 201 intervals come from the outermost margin of the 2014–2015 Holuhraun eruption (Figure 1f),
 202 which was extensively studied while active (e.g., Kolzenburg et al., 2017; Pedersen et al., 2017).
 203 The level, easily traversable sand sheet adjacent to a portion of this margin enabled us to collect
 204 an uninterrupted interval nearly 19 km long (ICE-01a).

205 Note that HAW-13a (Figure S1 of Supporting Information) is unique in the present study
 206 as it is the only margin interval that delineates the boundary between two subtypes within the
 207 same flow. Namely, HAW-13a represents the edge of a subtype of spiny pāhoehoe that Rowland
 208 and Walker (1987) called “primary toothpaste lava.” The surface of this subtype forms a series of
 209 plates and is surrounded by other forms of spiny lava (Rowland & Walker, 1987). Although not
 210 strictly a flow margin, HAW-13a mostly aligns with the margin of the largest primary lobe
 211 mapped by Rowland and Walker (1987) (their Figure 1) and could plausibly be misinterpreted as
 212 a flow margin in remotely-sensed data. This margin interval therefore provides a useful reference
 213 to evaluate the potential for lava flow characterization in the absence of ground truth.

214 2.2.3 Block–‘a‘ā (Highway flow)

215 Finally, we include a margin interval from a lava that may be intermediate between block
 216 lava and ‘a‘ā. This interval (IDA-01) comes from the margin of the informally named
 217 “Highway” flow (Figure 1h) at Craters of the Moon National Monument and Preserve in Idaho,
 218 USA (Hughes et al., 2019; Kuntz et al., 1982; Tolometti et al., 2020).

219 Classic block lavas have thicknesses of tens or even hundreds of meters and are covered
 220 in angular blocks or sub-rounded boulders (Harris et al., 2017). Their surface is generally
 221 vesicle-poor but may have highly vesicular bands (Harris et al., 2017). Highway flow is ~15 m
 222 thick. Its surface includes both rough, viscously-torn slabs, analogous to ‘a‘ā clinker, and

223 fractured blocks (Hughes et al., 2019; Kuntz et al., 1982; Tolometti et al., 2020). This surface
224 generally has low vesicularity but isolated regions of high vesicularity are exposed on ~1–2% of
225 the surface (Hughes et al., 2019; Sandmeyer et al., 2017).

226 This flow is among the most evolved of those tested in the area. Chemical analyses
227 typically measure ~62–65 wt% SiO₂ (Kuntz et al., 1985; Leeman et al., 1976; Stout et al., 1994;
228 Tolometti et al., 2020) and qualify the flow as a trachyte or trachydacite (Stout et al., 1994;
229 Tolometti et al., 2020). Although lavas on Mars, for example, generally have more primitive
230 compositions than that of Highway flow, Christensen et al. (2005) measured ~60–63% SiO₂ for
231 one flow using data from the Thermal Emission Imaging System on board Mars Odyssey
232 (Christensen et al., 2004). The alpha proton x-ray spectrometer on the Mars Pathfinder rover also
233 measured rocks in situ with similar SiO₂ content (Economou, 2001; Rieder et al., 1997).

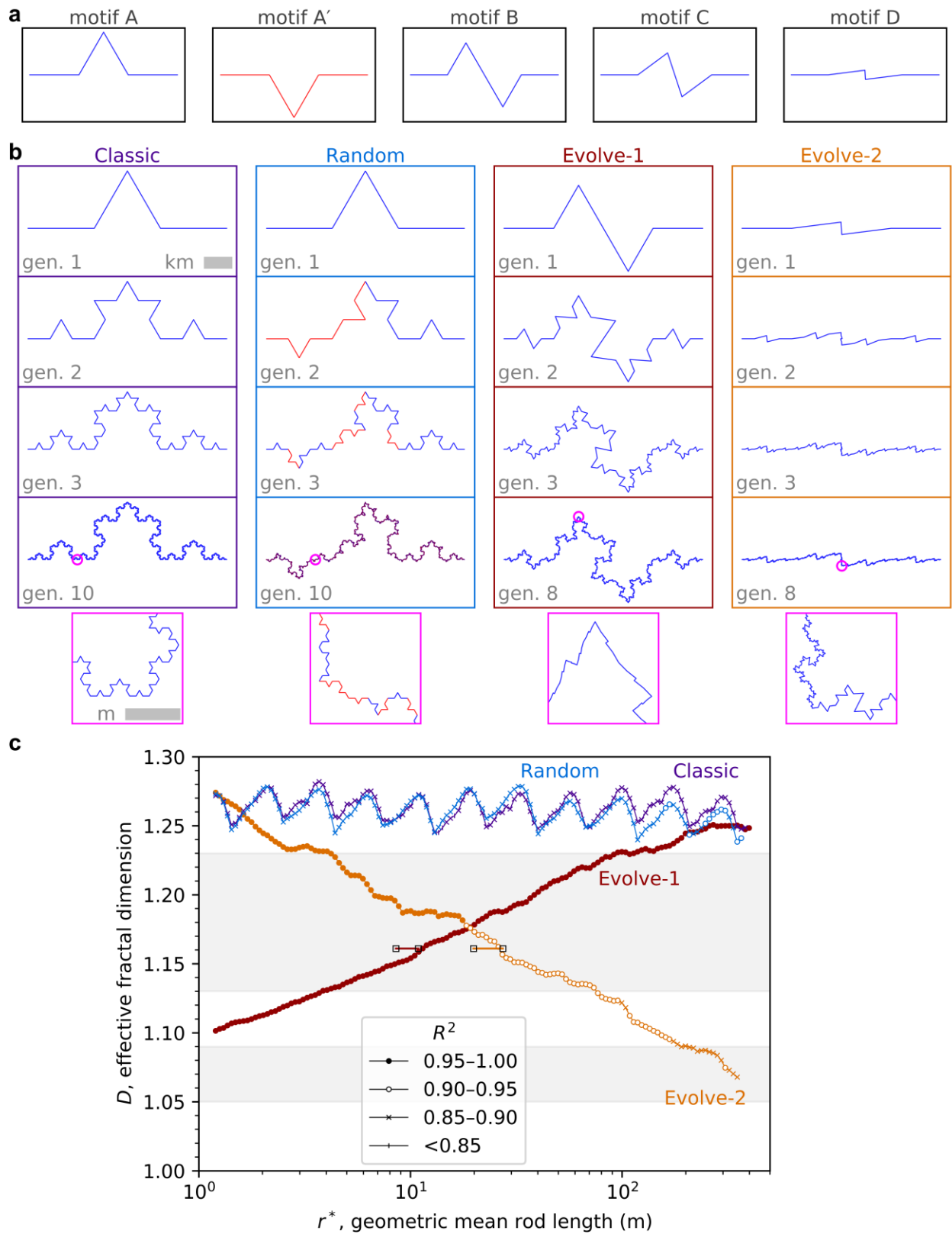
234 As the single non-mafic margin interval in the present study, the results for IDA-01
235 cannot be confidently interpreted as general. Nonetheless, these results provide a valuable
236 supplement to the results of other workers at different scales (Bruno et al., 1994; Pyle & Elliott,
237 2006; Wroblewski et al., 2019).

238 2.3 Topographic context

239 There is generally a paucity of meter-scale topographic data available for planetary
240 surfaces, and in high-resolution visual images, shadowing suggestive of the topographic context
241 may be absent if relief is subtle or lighting conditions are ill-suited. Therefore, it may not be
242 possible to independently identify the presence of topographic confinement or significant slopes
243 at meter scales for these locations. Even where sufficiently high-resolution topographic data are
244 available (e.g., Kirk et al., 2008; Moratto et al., 2013; Shean et al., 2016), knowledge of the
245 respective effects of slopes and confinement on empirical margin fractality is essential to
246 interpreting flows in those settings.

247 Bruno et al. (1994) examined three margin intervals on significant slopes. All three
248 intervals came from 1972 Mauna Ulu ‘a‘ā flows on respective slopes of 11.6°, 14.7°, and 27.8°.
249 Bruno et al. (1994) reported significant modification of empirical fractality only for the margin
250 on the steepest slope and therefore inferred a critical slope angle in the range 15–28°. To further
251 explore the lower end of this range and determine whether any modification of empirical
252 fractality has a scale-dependent component, we include in the present study a 1971 Mauna Ulu
253 ‘a‘ā flow on a slope of ~15° (HAW-15).

254 The potential for topographic confinement to modify margin fractality has long been
255 recognized (Bruno et al., 1992). However, to our knowledge, no fractal analysis of such a
256 topographically-confined margin has yet been reported. We therefore collected a second
257 Holuhraun margin interval (ICE-02; inset of Figure 1f) that was strongly confined by the right
258 bank of a preexisting stream channel (Bonney et al., 2019). Because both Holuhraun intervals
259 are dominated by spiny pāhoehoe (Voigt et al., 2017), comparison of the confined and relatively
260 unconfined intervals facilitates direct evaluation of the effects of topographic confinement.



261
 262 **Figure 2.** Construction and fractal analysis of some illustrative synthetic geometries. (a)
 263 Example motifs used in constructing the geometries. (b) Each geometry is constructed
 264 iteratively: generation 1 is a motif from (a), and in each successive generation, every line

265 segment is replaced by a motif. Classic uses only motif A. For Random, motif A and its flipped
 266 counterpart motif A' each have a 50% chance of replacing any segment. Evolve-1 begins with
 267 motif B at generation 1, but the motif used at each later generation evolves, by incrementally
 268 shortening the middle segment, passing through motif C and culminating with motif D at
 269 generation 8. Evolve-2 has the opposite sequence, beginning with motif D and progressing
 270 through motif C to motif B at generation 8. Each final geometry has mean segment lengths of
 271 11.8–12.4 cm. All segment lengths are equal for Classic and Random but vary by a factor of 70
 272 for Evolve-1 and Evolve-2 at generation 8. This variation is evident in the magenta-outlined
 273 magnified views, which have equal map scale. (c) The results of scale-dependent fractal analysis,
 274 or “fractal scale-spectra”, for the final geometries from (b). The theoretical fractal dimension
 275 value for both Classic and Random is $D = \frac{\ln(4)}{\ln(3)} \cong 1.26$ (Mandelbrot, 1967), which is reasonably
 276 approximated by the analysis. (See also Figure S2 of the Supporting Information.) Motif C is
 277 applied at generation 4 for Evolve-1 and at generation 5 for Evolve-2, and has a theoretical $D =$
 278 $\frac{\ln(5)}{\ln(4)} \cong 1.16$ (Mandelbrot, 1967). For Evolve-1 and Evolve-2, a horizontal line at this D value is
 279 drawn between the mean and median segment lengths of the corresponding generation. The
 280 intersection of these horizontal lines with the Evolve-1 and Evolve-2 scale-spectra suggests that
 281 r^* is a reasonable approximation of the scale to which the measured D is sensitive. The pale gray
 282 bands are as in Figures 4–6, for reference, and markers indicate R^2 values (section 3.2.2).

283

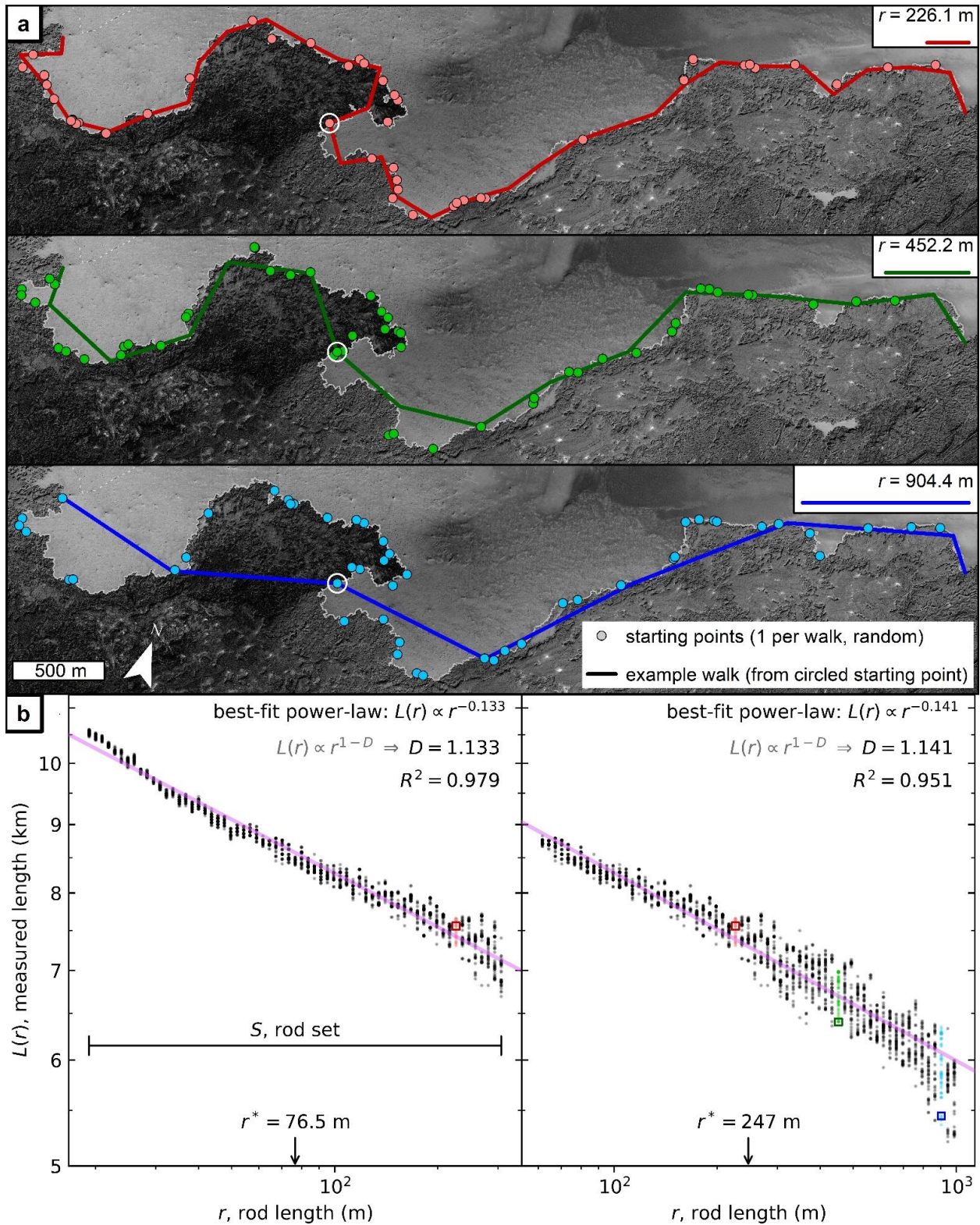
284 **3 Methods**

285 3.1 Field measurement techniques

286 To collect margin interval vertices in the field, we used differential global navigation
 287 satellite system (differential GNSS) receivers to collect margin interval vertices. We used two
 288 GNSSs: the Global Positioning System (GPS) and the Global Navigation Satellite System
 289 (GLONASS).

290 We walked the length of each margin interval with a differential GNSS rover while a
 291 differential GNSS base station simultaneously collected data. In each case, the rover and base
 292 station were both Trimble R8s or both Trimble R10s. Depending on the reliability of line-of-
 293 sight communication between the rover and base station, we used a sampling interval that was
 294 either spatial (e.g., collect one vertex every 10 cm), which requires continuous line-of-sight
 295 communication to support a real-time kinematic correction, or temporal (e.g., collect one vertex
 296 each second). Table 1 records the resulting variability in inter-vertex spacing.

297 We postprocessed each vertex using the Trimble Business Center software. The reported
 298 horizontal precision is ≤ 3 cm for all vertices. However, we observed the rover mast to slightly
 299 tilt at times and estimate our mean measurement error relative to the true margin to be ~ 15 cm
 300 (corresponding to a tilt of $\sim 4^\circ$). We provide evidence that this estimate is reasonable in section
 301 S1 of Supporting Information. To better simulate the plan-view geometry of orthorectified or
 302 nadir-pointing images, all analyses use only the x - and y -coordinates of the postprocessed
 303 vertices.



304
 305
 306
 307
 308

Figure 3. Examples from the fractal analysis of margin interval ICE-01a by the divider method (section 3.2.2). (a) Example data for three different rod lengths. ICE-01a is drawn in light gray. Background is 2015 visible data from Loftmyndir ehf. (0.5 m/pixel). For each rod length, the random starting points for all 50 walked paths are shown as colored dots. Also shown is a single

309 example path walked with each rod length, starting from the white-circled starting point in each
 310 pane. (b) Two log–log Richardson plots. Each shows 50 measured lengths (with each length
 311 measured from a different starting point) for each of 65 different rod lengths. The 65 rod lengths
 312 in each plot form a rod set. The three selected rod lengths (r values) and their colors correspond
 313 in (a) and (b), with the example walks from (a) marked by squares in (b). The representative
 314 scale, r^* , is the geometric mean rod length for each rod set (Richardson plot), or equivalently,
 315 the median rod length. The effective fractal dimension D is calculated from the trend (which is
 316 linear in a log-log plot) of the best-fit power-law (pastel purple), as indicated. The coefficient of
 317 determination R^2 measures the goodness of fit and has a maximum of unity (section 3.2.3). The
 318 compiled D values from many rod sets analyzing the same margin interval form a fractal scale-
 319 spectrum (e.g., Figure 2c). Two Richardson plots are shown to (1) highlight the reuse of results
 320 for the same rod length r between different rod sets, such as the results for $r = 226.1$ m (red
 321 dots), which appear in both plots, and (2) provide examples of two different R^2 values.
 322

323 3.2 Fractal analysis

324 3.2.1 Natural fractality

325 How the measured fractality of natural geometries should be interpreted has been debated
 326 (e.g., Avnir et al., 1998; Shenker, 1994). Early workers (e.g., Mandelbrot, 1967) interpreted such
 327 fractality to imply statistical self-similarity. In strictly self-similar geometries, such as the classic
 328 Koch curve (Classic in Figure 2), identical geometric patterns are observed when the fractal is
 329 viewed across a wide range of scales (Mandelbrot, 1967). For a statistically self-similar
 330 geometry, on the other hand, comparable but not identical geometric patterns repeat across a
 331 wide range of scales. The random Koch curve (Random in Figure 2) is one such example
 332 (Falconer, 2003).

333 More recently, Mandelbrot (2002) urged greater caution in interpreting natural
 334 geometries to be self-similar. Additionally, Gneiting and Schlather (2004) presented a family of
 335 synthetic geometries that have formally-defined fractality but are not self-similar, and Li and Li
 336 (2017) have since used this family to describe natural phenomena, namely, sea level fluctuations.
 337 In this work, we interpret measured fractality to describe the tortuosity of a line rather than imply
 338 statistical self-similarity. Likewise, we interpret the effective fractal dimension D as a summary
 339 statistic that describes tortuosity over a scale range.

340 3.2.2 Overview of the divider method

341 Different fractal analysis methods can yield different effective fractal dimension (D)
 342 values (e.g., Gneiting et al., 2012; Klinkenberg & Goodchild, 1992). Moreover, such
 343 discrepancies have been specifically reported for lava flow margins (cf. Bruno et al., 1994;
 344 Gaonac'h et al., 1992; Luongo et al., 2000). We choose to use the divider method to support
 345 comparison to both the large catalog of Bruno et al. (1994) and to most other studies of lava
 346 margin fractality (e.g., Blake & Bruno, 2000; Bray et al., 2018; Pyle & Elliott, 2006; Wroblewski
 347 et al., 2019).

348 In the simplest version of the divider method (Figure 3) (Richardson, 1961), a rod of a
 349 specified length r_1 is walked along the length of a geometry—for example, a lava margin—such
 350 that each end of the rod touches the margin with each step. For each step after the first, the start

351 of the rod is anchored to the location where the rod ended in the previous step. (Note that the
 352 interior of the rod—between its ends—is allowed to intersect the margin.) The apparent length
 353 $L(r_1)$ of the geometry, as measured by the rod, is recorded. This same procedure is then repeated
 354 with n different rods, each of a different length r_i . If the apparent lengths $L(r_i)$ versus the
 355 respective rod lengths r_i used to make those measurements follow a power-law decay, the
 356 effective fractal dimension D can be calculated from the best-fit $L(r) \propto r^{1-D}$. Equivalently,
 357 these measurements would follow a linear trend with negative slope m on a log–log plot (Figure
 358 3b)—often called a Richardson plot in this context—and the fractal dimension could be
 359 calculated from $D = 1 - m$.

360 When walking a rod along a margin, it is possible that multiple points in the walking
 361 direction are exactly a distance r_i from the rod’s start. In this case, our implementation invariably
 362 uses the first such point, which Mandelbrot (1986) referred to as a “first exit.” An
 363 implementation may instead invariably use the last such point, or “last exit.” The respective D
 364 values calculated by first- and last-exit walks are only guaranteed to be equal for self-similar
 365 fractals (Mandelbrot, 1986). We adopt the convention to use first exits because Bruno et al.
 366 (1992, 1994) adopted this same convention, both in their field and photographic analyses, the
 367 latter of which used the EXACT algorithm (Hayward et al., 1989). The first-exit convention is
 368 also more computationally efficient (Klinkenberg, 1994).

369 Following previous workers (e.g., Bruno et al., 1994), we interpret a lava flow margin
 370 interval to be empirically fractal if the best-fit $L(r) \propto r^{1-D}$ reasonably describes the trend of the
 371 data, as quantified by the coefficient of determination R^2 . Throughout this work, we use
 372 “empirical” or “measured” fractality to signal this interpretation of fractality and distinguish it
 373 from analytical definitions (cf. Falconer, 2003; Mandelbrot, 1982). Similarly, and following
 374 Mandelbrot (1982), we refer to fractal dimensions determined by measurement rather than from
 375 theory as effective fractal dimensions but use the variable D for both theoretical and effective
 376 fractal dimensions. To calculate R^2 , we use the formula:

$$377 \quad R^2 = 1 - \frac{\sum_{i=1}^n (\hat{y}(r_i) - y_i)^2}{\sum_{i=1}^n (y_i - \bar{y})^2}, \quad [\text{Eq. 1}]$$

378 which supports comparison between linear and nonlinear fits and is one of the formulae
 379 recommended by Kvålseth (1985). We perform model fitting using the version of the
 380 Levenberg–Marquardt algorithm described by Moré (1978), as implemented in SciPy, a
 381 scientific computing package in the Python programming language.

382 3.2.3 Selection and stepping of rods

383 To avoid overrepresenting the inter-vertex segments or measurement error in our results,
 384 we set the shortest rod used for each margin interval equal to the larger of twice the mean inter-
 385 vertex spacing (Andrle, 1992) (Table 1) and twice the estimated measurement error of ~ 15 cm
 386 (section 3.1 and section S1 of Supporting Information). Each successively longer rod has a
 387 length $r_i = f r_{i-1}$, where $f > 1$. Such geometric spacing is generally used in fractal analysis
 388 (Klinkenberg, 1994) and reflects the scaling of empirical fractals. Following Bruno et al. (1992,
 389 1994), the largest rod used for each margin interval must walk that interval in no fewer than five
 390 steps (including the fractional steps described in the next paragraph).

391 With each rod (Figure 3a), we start walking at a randomly selected point along the
 392 margin interval (which is generally not at a vertex) to avoid overrepresenting any particular
 393 subset of coordinates (Andrle, 1992). Once the rod has been walked to the end of the margin

394 interval, we restart walking from the randomly-selected point in the opposite direction and sum
 395 the lengths measured in each direction (Andrle, 1992). When the final step of a walk would
 396 overshoot the end of a margin interval (as is generally the case), the residual straight-line
 397 distance to the end vertex is added to the measured length. This addend is intended to mitigate
 398 systematic error (Andrle, 1992; Klinkenberg, 1994). The entire procedure is then repeated 49
 399 more times with each rod, each time from a newly selected random point, following Andrle
 400 (1992).

401 3.2.4 Rod sets and rod set sequences

402 The scale dependence of the effective fractal dimension D is a major focus of the present
 403 study but has not been emphasized in previous studies of lava margins (section 2.1) or other
 404 geomorphic features (Andrle, 1996b, 1996a). D must be calculated over a range of scales.
 405 Therefore, to describe the scale dependence of D , we must calculate D over many scale ranges
 406 for each margin interval. Each such scale range is defined by the range of rod lengths used in the
 407 analysis. We refer to the sequence S of rod lengths r that span such a scale range as the “rod set”
 408 for that analysis (Figure 3b). Thus, for each analysis k , which yields a single D value, $S_k =$
 409 $(r_{i=1}, r_{i=2} \dots r_{i=n})|_k$. For simplicity of reference, and following Andrle (1992), we will treat the
 410 geometric mean of a rod set $r^* = (\prod_{i=1}^n r_i)^{1/n}$ as the representative scale of that rod set. Because
 411 each rod set in the present study is composed of an odd number ($n = 65$) of logarithmically-
 412 spaced rod lengths, r^* is also the median rod length of each rod set. Although r^* is a non-
 413 rigorous convenience, it provides a plausible reference value (Figure 2c).

414 To define a rod set, any two of three interdependent parameters must be specified: the
 415 inter-rod factor $f = r_{i+1}/r_i$, the number of rods n in the rod set, and the factor-range of the rod
 416 set $F = r_n/r_1$. Andrle (1992) observed that a larger n reduced random scatter in the calculated D
 417 values but also noted that a larger F would yield a poorer model fit in the presence of any
 418 systematic divergence from a power-law trend (e.g., curvature on a Richardson plot; Figure 3b).
 419 On that basis, he suggested the use of a large n and a small F . However, we interpret D as a
 420 summary statistic that describes tortuosity over a scale range, roughly analogous to a moving
 421 average of scale-dependent tortuosity (where the averaging window moves along the r^* axis). In
 422 that interpretation, F should be sufficiently large to avoid variability due to random noise but not
 423 larger than that, to preserve as much scale resolution as possible and support as many rod sets as
 424 possible for a given geometry.

425 Guided by these goals, we use $F = 16$ and $n = 65$, implying $f = F^{1/(n-1)} = 16^{1/64} \cong$
 426 1.044 , throughout the present study. These parameters satisfy the recommendation $n \geq 5$ of
 427 Klinkenberg (1994) and facilitate comparison to the field analysis results of Bruno et al. (1994),
 428 who preferred $F = 16$ or 32 , $n = 5$ or 6 , and $f = 2$ for margin intervals as long as those in the
 429 present study (section 2.1). Each D value is therefore calculated by fitting 3250 apparent lengths
 430 (Figure 3b), which come from 50 iterations with each of 65 rod lengths in a rod set. The D value
 431 for each rod set is plotted against r^* on a log–log plot. We call the entire sequence of scale-
 432 dependent D values plotted for a given margin interval a “fractal scale-spectrum” (cf. Figure 7 of
 433 Andrle (1992) and Figure 4 of Maria and Carey (2002)). For example, the fractal scale-spectra in
 434 Figure 2c reflect how the tortuosity of Evolve-1 and Evolve-2 vary with scale.

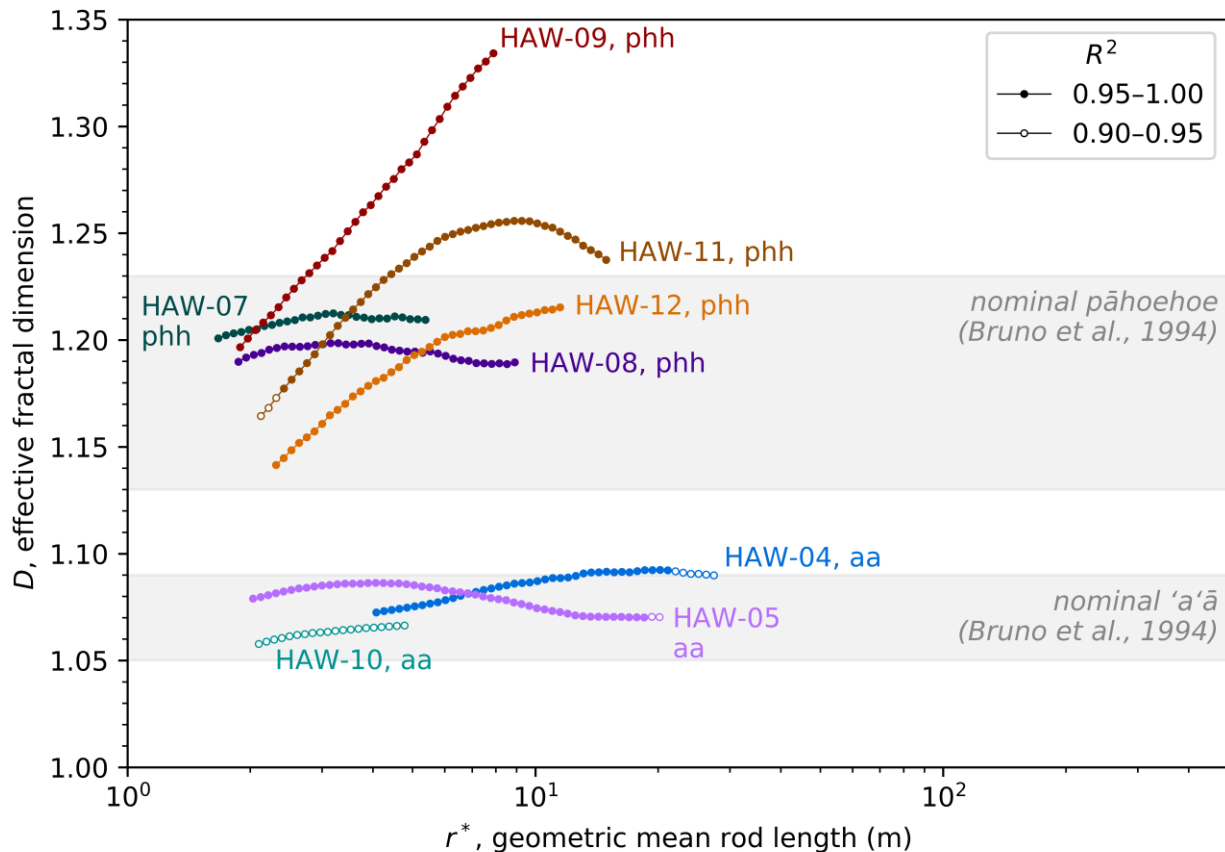
435 The ratio between the corresponding scales (e.g., minimum, maximum, representative) of
 436 consecutive rod sets is the inter-rod-set factor $I = (r_i|_{k+1})/(r_i|_k)$. We invariably set $I = f$

437 throughout this study. This correspondence permits rod-stepping results to be reused between
 438 overlapping rod sets, because $r_i|_k = r_{i-1}|_{k+1}$ (e.g., red dots in both plots of Figure 3b). This
 439 reuse facilitates an extreme savings in computation time. Unfortunately, this reuse also reduces
 440 the independence of D values calculated with overlapping rod sets. Nonetheless, the use of 50
 441 iterations (starting points) sufficiently reduces variability in calculated D values (Andrle, 1992)
 442 that the reuse of rod-stepping results has no significant effect on our general results.

443 3.2.5 Comparison to the Hurst exponent

444 For reference, we note another measure, called the Hurst exponent. The Hurst exponent
 445 has been used to characterize rough geologic surfaces in both terrestrial and planetary contexts
 446 (Neish et al., 2017; Shepard et al., 1995, 2001). Though fractality is often discussed when
 447 applying the Hurst exponent, the measure is generally independent of fractality (Gneiting &
 448 Schlather, 2004). Nonetheless, in the special case of self-similar geometries (section 3.2.1), the
 449 Hurst exponent H is simply related to D by $D = H - 3$ for surfaces and $D = H - 2$ for profiles
 450 (e.g., Shepard et al., 1995).

451



452 **Figure 4.** Fractal scale-spectra for 'a'ā (HAW-04, -05, and -10) and pāhoehoe (HAW-07, -08, -
 453 09, -11, and 12) margin intervals compared to nominal ranges (shaded gray) for 'a'ā and
 454 pāhoehoe from Bruno et al. (1994). None of these margin intervals have acute topographic
 455 effects. See Table 1 for explanation of morphologic codes (e.g., phh).
 456

457

458 **4 Results**

459 The fractal analysis results for ‘a‘ā and pāhoehoe margin intervals on shallow slopes
 460 (generally $\lesssim 4^\circ$), that lack substantial topographic confinement, are presented in Figure 4. The
 461 results for other morphologic types that likewise are not subject to acute topographic effects are
 462 presented in Figure 5. Finally, the results for an ‘a‘ā margin interval on a 15° slope (HAW-15)
 463 and a spiny pāhoehoe margin interval confined by a stream channel (ICE-02) are presented in
 464 Figure 6. In these plots, scale-invariant behavior is indicated by a constant fractal dimension D as
 465 the geometric mean rod length r^* changes, and hence, a horizontal trend. Conversely, scale-
 466 dependent behavior is indicated by variation in D as r^* changes.

467 **4.1 Scale dependence**

468 In general, the examined margin intervals exhibit a wide range of scale-dependent to
 469 relatively scale-independent empirical fractal behavior. For discussion purposes, we will adopt
 470 the criteria of Bruno et al. (1994) in this section to identify scale-dependent empirical fractality.
 471 Bruno et al. (1994) discarded all fractal analyses for which $R^2 \leq 0.95$ or for which slope or
 472 topographic confinement are significant. Twelve margin intervals satisfy these criteria. Bruno et
 473 al. (1994) further interpreted empirical fractality to be scale-independent if the observed
 474 variation in D was $\lesssim 0.05$. Based on that criterion, 7 of the remaining 12 margin intervals
 475 (HAW-04, HAW-05, HAW-07, HAW-08, HAW-13a, IDA-01, and IDA-03) have scale-
 476 independent empirical fractality, with observed D variation of 0.01–0.05, and 5 (HAW-09,
 477 HAW-11, HAW-12, ICE-01a, and IDA-02) have scale-dependent empirical fractality, with
 478 observed D variation of 0.07–0.17. For reference, note that relaxing the minimum required R^2 to
 479 0.90 (Anderson et al., 2005; You et al., 1996) would cause 13 margin intervals to be included:
 480 HAW-10 would be added to the list of scale-independent margin intervals (Figure 4) and IDA-03
 481 and HAW-13a would switch from scale-independent to scale-dependent, with D variations of
 482 0.08 and 0.06, respectively (Figure 5).

483 Returning to the $R^2 > 0.95$ criterion, all five of the margin intervals with scale-
 484 dependent empirical fractality have a maximum effective fractal dimension $D_{\max} \gtrsim 1.19$. The
 485 fact that margin intervals with lower D_{\max} values do not exhibit greater variation in D may
 486 partially reflect their proximity to the lowest possible value $D = 1$. However, one cannot
 487 generalize that margin intervals with low D values have little variation in D and margin intervals
 488 with high D values have large variation in D . For example, D values measured for IDA-02 range
 489 from the relatively low $D_{\min} \approx 1.08$ at $r^* \approx 1.20$ m to the relatively high $D_{\max} \approx 1.25$ at $r^* \approx$
 490 35.2 m, a span of ~ 0.17 . For comparison, 24 of the 27 margin intervals measured by Bruno et al.
 491 (1994) in the field fall in the same range of D values, 1.08–1.25, measured for IDA-02 alone,
 492 including all pāhoehoe and transitional margin intervals and most (4 of 7) ‘a‘ā margin intervals.
 493 At the other extreme of variability, two pāhoehoe intervals from the same margin on Mauna Ulu,
 494 HAW-07 and HAW-08, each have D values that vary by ~ 0.01 across the analyzed scales (r^* of
 495 1.67–5.37 m and r^* of 1.87–8.90 m, respectively), despite having $D_{\min} \gtrsim 1.20$.

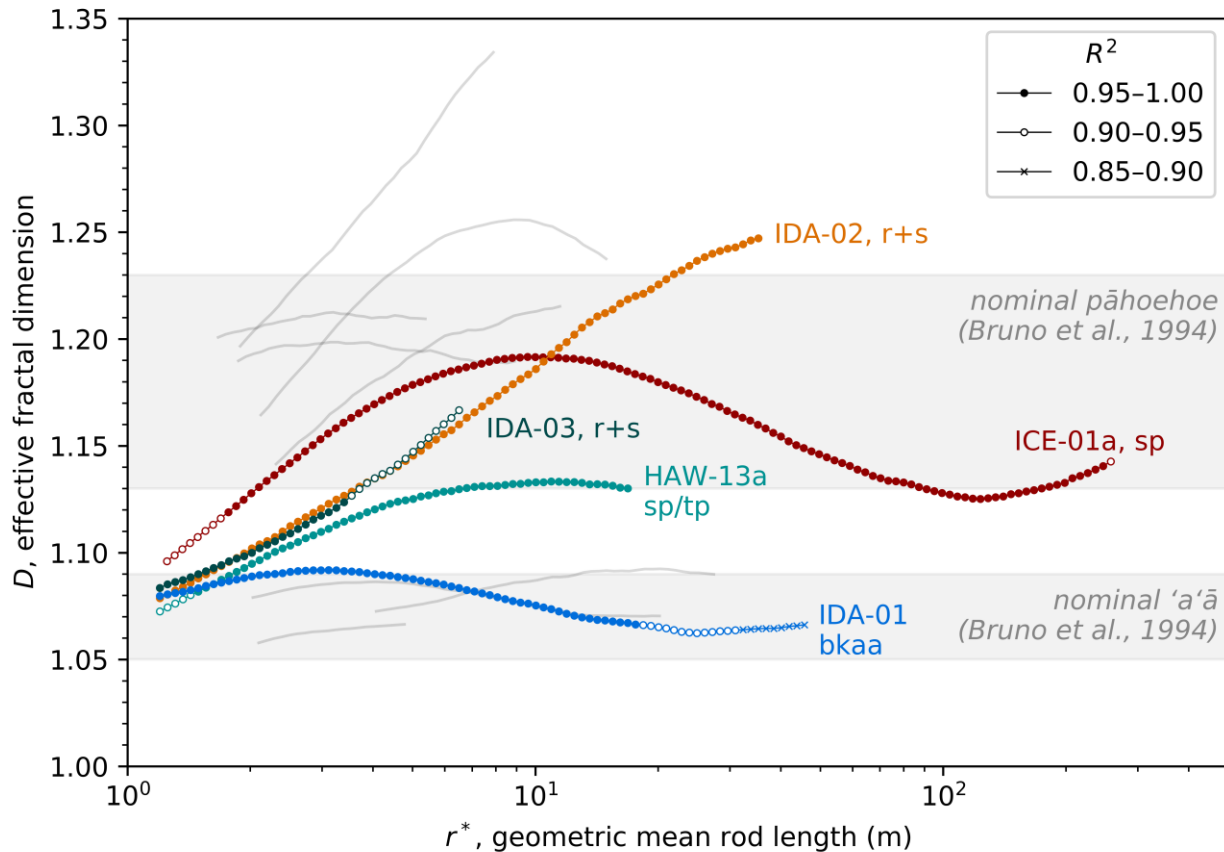
496 **4.2 Topographic effects**

497 Two margin intervals are subject to acute topographic effects and therefore violate what
 498 Bruno et al. (1994) called their “simple-case” criteria (Figure 6). To enable some useful
 499 comparisons, we will only exclude in the present section those results for which $R^2 \leq 0.90$,
 500 similar to You et al. (1996) and Anderson et al. (2005). Nonetheless, the general behavior

501 described here is at least suggested by those results that meet the more restrictive $R^2 > 0.95$
 502 criterion (cf. section 4.1).

503 Compared to the other three ‘a‘ā margin intervals, HAW-15, on a slope of 15° , has much
 504 lower D values. Its D_{\max} is 1.05, measured at $r^* = 1.20$ m. No other margin interval in this
 505 study, except for the topographically-confined ICE-02, has a D value as low at any analyzed
 506 scale, and the lowest D value measured by Bruno et al. (1994) on a slope $\leq 15^\circ$ was likewise 1.05.
 507 HAW-15’s D_{\min} is 1.02, measured at $r^* = 16.9$ m, which is the lowest D measured in the
 508 present study. The lowest D reported by Bruno et al. (1994) was also 1.02 and was measured for
 509 another Mauna Ulu ‘a‘ā margin interval on a 28° slope.

510



511 **Figure 5.** Fractal scale-spectra for spiny pāhoehoe (ICE-01a), block-‘a‘ā (IDA-01), rubbly and
 512 slabby lava (IDA-02 and IDA-03), and primary toothpaste (HAW-13a) margin intervals, with
 513 fractal scale-spectra from Figure 4 shown as unmarked gray lines, for comparison. None of these
 514 margin intervals have acute topographic effects. See Table 1 for explanation of morphologic
 515 codes (e.g., r+s).
 516

517

518 D values for the Holuhraun margin interval confined by a stream channel, ICE-02, are
 519 likewise much lower than D values measured at the same scales for the relatively unconfined
 520 Holuhraun margin interval, ICE-01a. Over r^* of 1.25–19.1 m, and requiring $R^2 > 0.90$, D values
 521 measured at equivalent scales are 0.037–0.146 less for ICE-02 than for ICE-01a. The respective

522 ranges of D values over those scales are also disjoint: D of 1.04–1.07 for ICE-02 but D of 1.10–
 523 1.19 for ICE-01a.

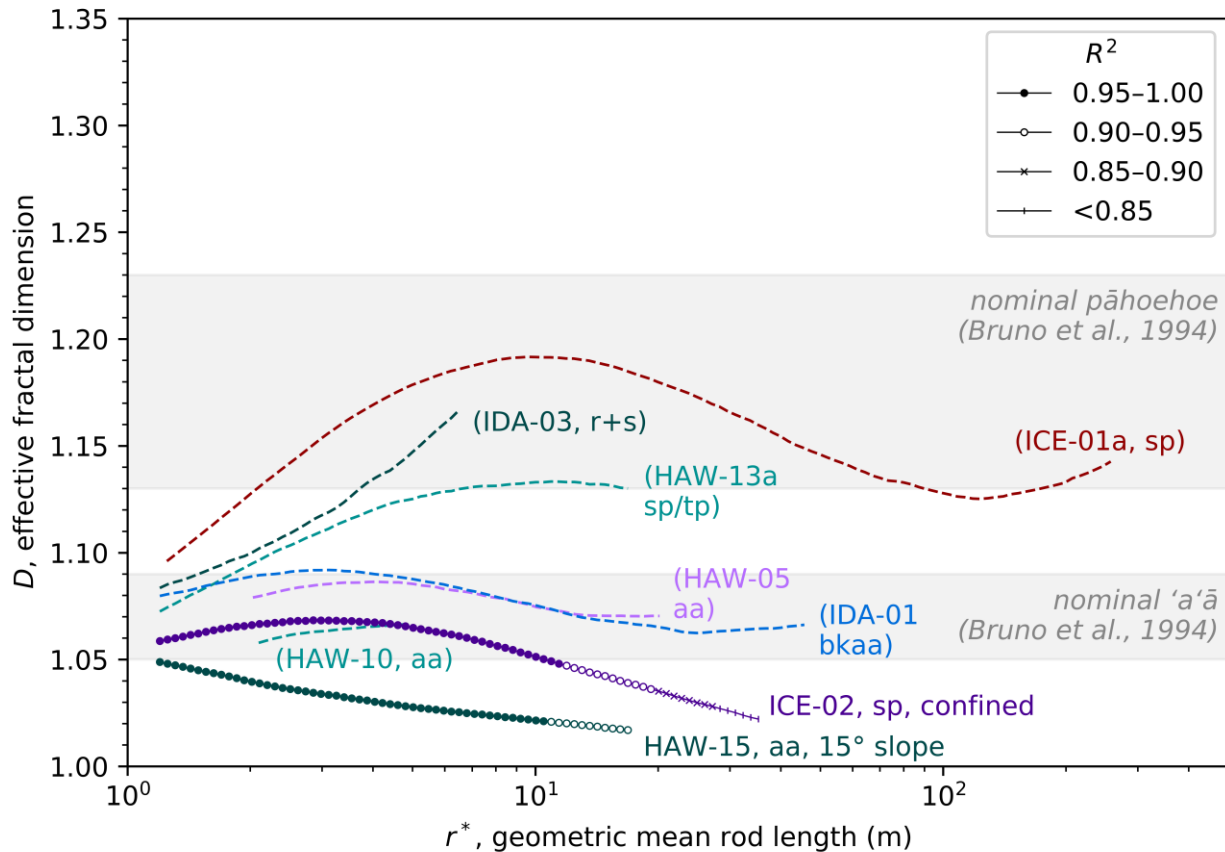
524 **5 Discussion**

525 5.1 Consequences for interpretation

526 5.1.1 Intrinsic variability of basaltic lava margins

527 Our analyses of ‘a‘ā and pāhoehoe margin intervals (Figure 4) reproduce the general
 528 results of comparable analyses by Bruno et al. (1994). Namely, these results are that ‘a‘ā and
 529 pāhoehoe margins have distinct typical D ranges that do not overlap, with the D values of
 530 pāhoehoe margins systematically higher than those of ‘a‘ā margins. Our results also largely
 531 reproduce the quantitative details of those of Bruno et al (1994). Their field analyses correspond
 532 to r^* of 0.5–4 m, with a preference for $r^* = 4$ m and $r^* = 2.83$ m (section 2.1). At $r^* < 4$ m,
 533 the results for our three ‘a‘ā intervals (after rounding to the nearest hundredth) all fall within the
 534 nominal ‘a‘ā range of 1.05–1.09 that Bruno et al. (1994) identify, though they would have
 535 rejected the results for HAW-10 for having $R^2 \leq 0.95$. Similarly, at these scales, only the results
 536 for HAW-09 of the five pāhoehoe intervals is outside the nominal pāhoehoe range of 1.13–1.23,
 537 at $r^* > 2.7$ m.

538



539 **Figure 6.** Fractal scale-spectra for ‘a‘ā margin interval on 15° slope (HAW-15) and spiny
 540 pāhoehoe margin interval that was confined by a preexisting stream channel (ICE-02).
 541

542 Additional fractal scale-spectra from Figures 4 and 5 for select margin intervals are shown as
 543 dashed lines with parenthetical labels and no markers, for comparison: spiny pāhoehoe ICE-01a,
 544 rubbly and slabby lava IDA-03, primary toothpaste HAW-13a, ‘a‘ā HAW-05, ‘a‘ā HAW-10, and
 545 block-‘a‘ā IDA-01. These additional margin intervals are on shallow slopes $\lesssim 4^\circ$ and relatively
 546 unconfined. See Table 1 for explanation of morphologic codes (e.g., r+s).

547

548 However, our results for other morphologic types significantly complicate this picture
 549 (Figure 5). Even if we consider only basaltic margins and exclude results for which $R^2 \leq 0.95$,
 550 every analyzed margin interval for a morphologic type other than ‘a‘ā and pāhoehoe has at least
 551 some D values in the nominal ‘a‘ā and/or pāhoehoe ranges of Bruno et al. (1994). Measured D
 552 values fall in the nominal pāhoehoe range for spiny pāhoehoe ICE-01a at r^* of 2.01–247 m
 553 (rounding D to the nearest hundredth), for rubbly and slabby lava IDA-02 at 3.07–21.9 m, and
 554 for primary toothpaste HAW-13a at 6.79–16.9 m. Similarly, D values fall in the nominal ‘a‘ā
 555 range for rubbly and slabby lava IDA-02 at r^* of 1.20–1.56 m, rubbly and slabby lava IDA-03 at
 556 1.20–1.49 m, and primary toothpaste HAW-13a at 1.49–1.78 m.

557 Taken together, the widely varying scale dependence of empirical margin fractality
 558 among the analyzed intervals and the frequently overlapping D ranges of the analyzed
 559 morphologic types indicate that D , when measured with a single rod set, is not a reliable,
 560 independent indicator of morphologic type at meter scales (that is, for r^* of ~ 1 –10 m). It further
 561 seems unlikely that the shape of the fractal scale-spectrum has the potential to serve as a
 562 discriminator of morphologic type at meter scales. For example, among pāhoehoe margin
 563 intervals, the fractal scale-spectra (Figure 4) for HAW-07 and HAW-08 (Figure 1c) are distinctly
 564 different from those of HAW-09 (Figure 1d), HAW-11, and HAW-12.

565 Moreover, primary toothpaste HAW-13a, which is the only interval along an internal
 566 subtype margin (section 2.2.2), does not have a distinguishing scale-spectrum. Although primary
 567 toothpaste is a subtype of spiny pāhoehoe, its scale-spectrum nearly coincides with that of rubbly
 568 and slabby lava IDA-03 over r^* of 1.49–3.39 m (excluding results with $R^2 \leq 0.95$) (Figure 5).
 569 The curvature of the HAW-13a scale-spectrum is also similar to that of the spiny pāhoehoe ICE-
 570 01a scale-spectrum, and the results for HAW-13a have high R^2 values (>0.90 and typically
 571 >0.95) similar to those for flow margin intervals. These observations suggest that subtype
 572 margins within flows may not be readily distinguished from flow margins by their fractality (cf.
 573 Anderson et al., 2005).

574 5.1.2 Margins of non-mafic composition

575 For block-‘a‘ā IDA-01, which has intermediate composition, we measure D values of
 576 1.07–1.09 for r^* of 1.2–17.6 m (which use r of 0.3–70.4 m). This result is in reasonable
 577 agreement with those of Bruno et al. (1994), who measured D values of 1.08–1.17 for $r < 31.6$
 578 m and 1.09–1.20 for r of 31.6–100 m among five margin intervals of basaltic andesite. (Bruno et
 579 al. (1994) do not specify the rods used and therefore r^* cannot be calculated.) At coarser scales,
 580 Bruno et al. (1994) measured systematically higher D values. For example, they reported D
 581 values of 1.20–1.46 for four of these margin intervals at r of 316–1995 m. They therefore
 582 concluded that margin intervals of intermediate composition, unlike those of mafic composition
 583 (cf. section 4.1), have scale-dependent fractality. Moreover, they speculated that lower D values

584 at fine scales may be due to the suppression of nonlinear flow dynamics at these scales, resulting
585 in non-fractality.

586 However, we note that the fractal scale-spectra for IDA-01, which has intermediate
587 composition, and HAW-05, which has basaltic composition, nearly coincide across their
588 overlapping scales, r^* of 2.03–20.3 m (requiring $R^2 > 0.90$) (Figure 6). This correspondence
589 suggests that margin intervals of intermediate composition are not necessarily less fractal than
590 those of basaltic composition and that fractal analysis may not be able to distinguish between
591 ‘a‘ā margin intervals, like HAW-05, and block-‘a‘ā margin intervals, like IDA-01. Similarly,
592 Pyle and Elliott (2006) concluded that fractal analysis with a single rod set cannot discriminate
593 between basaltic ‘a‘ā margins and dacitic block-‘a‘ā margins based on analysis of 10 dacitic
594 block-‘a‘ā margin intervals from the Kameni Islands, Greece at $r^* = 10$ m (r of 1–100 m). In
595 addition, Wroblewski et al. (2019) calculated single- r^* D values of 1.03–1.11 at r^* of 152–802
596 m for five subaerial margin intervals of intermediate to felsic composition. It is not currently
597 clear how these relatively low D values relate to the higher D values measured by Bruno et al.
598 (1994) at similar (coarse) scales and for similar compositions.

599 5.1.3 Topographic context

600 Interpretation of morphologic type from margin fractal analysis is further complicated by
601 topographic context (Figure 6). The margin interval from a Mauna Ulu ‘a‘ā flow on a 15° slope,
602 HAW-15, generally has very low D values. These D values are lower than those of any other
603 margin interval in the present study and lower than any result of Bruno et al. (1994) for a margin
604 interval on a shallower slope. These observations strongly suggest that HAW-15’s D values are
605 depressed relative to the intrinsic D of an ‘a‘ā margin interval. That is, these are lower than the D
606 values that would be expected for a similar flow margin interval on a shallow slope without
607 topographic confinement.

608 Similarly, Bruno et al. (1994) measured their lowest D value, 1.02, for another Mauna
609 Ulu ‘a‘ā margin interval on a 28° slope. Based on that observation, they likewise inferred that
610 steep slopes could depress D values. However, they also calculated an unusually low $R^2 = 0.78$
611 for that interval. This result led them to conclude that empirical “fractal behavior... break[s]
612 down, with an accompanying decrease in D , on steep (>15–28°) slopes.” Conversely, the results
613 for HAW-15 have $R^2 > 0.95$ across most analyzed scales (namely, for r^* of 1.20–10.5 m).
614 These high R^2 values indicate that a margin’s D can be significantly depressed by steep slopes
615 without an associated loss of empirical fractality. Interestingly, Bruno et al. (1994) measured
616 their two lowest D values at field scales for two Mauna Ulu ‘a‘ā margin intervals on slopes of
617 11.6° and 14.7°, with $R^2 = 0.99$ for both results. These observations could likewise suggest
618 depressed D values combined with retention of empirical fractality, though the intrinsically low
619 D values of ‘a‘ā margins complicates that interpretation.

620 Comparison of the results for spiny pāhoehoe ICE-02, which is confined by a channel, to
621 those of its relatively unconfined counterpart, ICE-01a, strongly suggests that the D values of
622 ICE-02 are also depressed. In addition, the results for ICE-02, like those for HAW-15, have
623 $R^2 > 0.95$ across meter scales (namely, for r^* of 1.20–11.4 m). However, the topographic relief
624 is distinctly different in each case. For HAW-15, flow is down dip and the 448 m margin interval
625 falls 88 m vertically along its length. For ICE-02, flow is along strike and parallel to a bank ~10
626 m high (Bonney et al., 2019, including their Figure 10). Moreover, when we observed the

627 margin in August 2015, the surface relief along portions of the interval was as low as ~2 m due
 628 to post-eruption fluvial modification (Bonnefoy et al., 2019, including their Figure 12).

629 The results for both HAW-15 and ICE-02 indicate that margin D values can be
 630 significantly depressed at meter scales by local topography without destroying empirical
 631 fractality. Therefore, low R^2 values for margin fractal analyses cannot be relied upon to
 632 recognize and exclude results modified by topography. In the absence of independent knowledge
 633 of local topography, a margin with low measured D may indicate a morphologic type with
 634 intrinsically low D , such as ‘a‘ā, or a morphologic type with intrinsically high D , such as
 635 pāhoehoe, that was topographically confined or emplaced on a slope. Moreover, even where
 636 topographic data are available, one must consider the potential that terrain adjacent to a lava
 637 margin was modified post-emplacment, as occurred along the ICE-02 interval. In the case of
 638 such modification, the extant surface relief could be below the vertical resolution of the data
 639 even if the original constraining height had been much greater.

640 5.2 Our results in context

641 5.2.1 Scale dependence

642 Our study focuses primarily on meter scales, that is, r^* of ~1–10 m. Only 6 of our 15
 643 fractal scale-spectra extend to scales of $r^* > 20$ m, and only the results for ICE-01a extend to
 644 $r^* \geq 100$ m.

645 Across meter scales, we observe significant variation in measured D values for 5 of the
 646 12 margin intervals that meet the selection criteria of Bruno et al. (1994) (section 4.1). (Of the 15
 647 margin intervals that we analyzed, Bruno et al. (1994) would have excluded HAW-15 and ICE-
 648 02, which are acutely affected by topography, and HAW-10, for which no measurement attained
 649 $R^2 > 0.95$.) At first glance, these results would appear to conflict with those of Bruno et al.
 650 (1994). Bruno et al. (1994) report no systematic differences in D between their 27 field analyses,
 651 which used r of 0.125–16 m and preferred $r^* = 4$ m and $r^* = 2.83$ m, and their 17 photographic
 652 analyses, which used r of 12–2400 m. For three margins, but different intervals, they also
 653 directly compared the D values measured in the field to those measured from photographs at
 654 coarser scales and found differences similar to along-length variations in D measured at a single
 655 r^* .

656 We propose that our results and those of Bruno et al. (1994) can be reconciled by
 657 considering measurement scale and methodology. Only the field analyses of Bruno et al. (1994)
 658 correspond to the meter-scale focus of our study. In those field analyses, Bruno et al. (1994)
 659 measured each margin interval with only a single rod set, and therefore, at a single r^* . These
 660 measurements are thus equivalent to sampling a single point from each fractal scale-spectrum
 661 (e.g., Figure 4). If these fractal scale-spectra vary as widely as those that we report, the scatter of
 662 the sampled D values would appear random. Consequently, the variability in measured D that
 663 Bruno et al. (1994) report between margin intervals may include scale-dependent variability as
 664 well.

665 5.2.2 Physical interpretation

666 Bruno et al. (1992, 1994) and Gaonac’h et al. (1992) interpreted basaltic flow margins to
 667 have scale-independent empirical fractality across decimeter to kilometer scales (see section

668 5.2.1). This interpretation led both them, and others (Anderson et al., 2005; Blake & Bruno,
669 2000; Kilburn, 1996), to either speculate on the physical implications of the inferred statistical
670 self-similarity or search for specific physical origins. However, even scale-independent empirical
671 fractality does not imply statistical self-similarity (section 3.2.1). Moreover, we measure scale-
672 dependent fractality for 5 of 12 suitable margin intervals at meter scales (section 4.1), and for
673 ICE-01a and IDA-02 at decameter scales. This scale dependence, as well as the broad range of
674 scale-dependent to relatively scale-independent behaviors that we observe, suggests that physical
675 insights based on the putative self-similarity of lava margins should be viewed with caution.
676 More generally, although fractal analysis facilitates quantitative descriptions of natural
677 geometries, it should not be interpreted to provide insight into the underlying physics unless such
678 an inference is independently supported by theory (e.g., Avnir et al., 1998; Neuman et al., 2013).

679 5.3 New interpretive framework

680 In section 5.1, we primarily highlighted the ways in which our results are not consistent
681 with the interpretive framework of Bruno et al. (1994). Nonetheless, there are also ways in which
682 our results correspond, at least approximately, to those on which Bruno et al. (1994) developed
683 their interpretive framework (e.g., the first paragraph of section 5.1.1). These points of
684 correspondence suggest that the underlying technique—namely, the fractal analysis of lava
685 margins—retains some of the same interpretive potential originally recognized by Bruno et al.
686 (1994). To realize this potential, we propose a modified framework that is informed by the new
687 insights, constraints, and sources of uncertainty identified by both the present study and other
688 recent research.

689 5.3.1 Flow suitability and recommended methods

690 Our framework draws primarily from two studies: the present one and that of Bruno et al.
691 (1994). Therefore, the best-suited flows are those that are compatible with the selection criteria
692 used in these studies, and the framework requires the use of similar methods.

693 The flows analyzed by Bruno et al. (1994) and in the present study (Table 1) are from
694 Earth, were emplaced subaerially, and are geologically young. These criteria imply a host of
695 conditions that can affect eruptions and flow emplacement but differ between planetary bodies,
696 such as gravitational acceleration, and/or with geologic time, such as atmospheric density,
697 ambient temperature, lava composition, and effusion rate (e.g., Self et al., 1998; Wilson & Head,
698 1994). We could conceivably expand the range of conditions sampled if we included submarine
699 lava flows from Earth, but the margin fractality of these flows has not been extensively studied
700 and existing results are ambiguous (Maeno et al., 2016; Mitchell et al., 2008; Wroblewski et al.,
701 2019). We therefore consider only young, subaerial terrestrial lava flows to be best suited to the
702 framework. Nonetheless, the utility of this framework to such lava flows suggests that margin
703 fractal analysis likely has value for studying lava flows in other environments and may facilitate
704 the identification of terrestrial analogs for flows on other planetary bodies.. For example, margin
705 fractal analysis could complement studies of planetary lava flows that have focused on
706 morphology, radar-derived surface roughness, and topographic roughness to relate those flows to
707 examples from Earth (Bruno & Taylor, 1995; Campbell & Campbell, 1992; Hamilton et al.,
708 2020; Keszthelyi et al., 2004; Tolometti et al., 2020; Whelley et al., 2017).

709 Best-suited flows are also geomorphically fresh and lack significant topographic
710 confinement. Any modification or obscuration of the margin by weathering, erosion, or mantling

711 would likely also modify the margin's meter-scale fractality. In the present study, the
 712 topographic confinement of ICE-02 significantly depressed its margin D (section 5.1.3).
 713 However, more generally, it is plausible that topographic confinement may either increase or
 714 decrease margin D depending on the fractality of the confining topography. For example,
 715 consider the extreme case in which the confining topography is very steep. In that case, the
 716 confining walls would effectively form a mold that is filled by the flow. This interpretation that
 717 the modification of margin D by confining topography depends on the geometry of that
 718 confining topography is consistent with our results for ICE-02. The stream channel that confines
 719 ICE-02 is smooth and straight relative to the tortuous geometry of the relatively unconfined ICE-
 720 01a, and that confinement depresses the margin D of ICE-02.

721 Measured fractal dimension values are sensitive to the method used and even to details of
 722 its implementation (section 3.2.2). Therefore, those who wish to use this framework are
 723 encouraged to use the same code as the present study (Schaefer, 2020b). Moreover, we only
 724 propose this framework for use at meter scales. The results of the present study explicitly
 725 consider scale, and the field-based results of Bruno et al. (1994) focus on a narrow range of
 726 scales. These combined results therefore describe 42 margin intervals at meter scales with
 727 sufficient detail so that scale dependence can be reasonably assessed. Conversely, the
 728 photographic analyses of Bruno et al. (1994) are scattered across a wide range of coarser scales,
 729 and with few exceptions, the relevant scales for each result are not reported. The results of the
 730 present study are also not well suited to explore those coarser scales (see section 5.2.1).

731 5.3.2 High margin D

732 For basaltic flows, Bruno et al. (1994) interpreted margin $D > 1.13$ to suggest pāhoehoe,
 733 We interpret margin $D \geq 1.13$ to be consistent with pāhoehoe at meter scales for best-suited
 734 flows but not uniquely indicative of that type, as transitional lava types may also have high
 735 margin D values at these scales (section 5.1.1). However, if a margin $D \geq 1.20$ is measured for a
 736 best-suited lava flow margin at meter scales, pāhoehoe is suggested, based on reported
 737 observations to date. All four of the pāhoehoe margin intervals in our study attain $D \geq 1.20$
 738 (rounded to the nearest hundredth) within r^* of 1–10 m, and no margin interval of another
 739 morphologic type attains such a high D value over these scales in the present study. Similarly,
 740 the only 4 basaltic margins that attain $D \geq 1.20$ at meter scales in the catalog of Bruno et al.
 741 (1994) are all pāhoehoe, though 11 more pāhoehoe margins have $D < 1.20$. Although Bruno et
 742 al. (1994) did not analyze non-mafic lava margin intervals at meter scales, they reported
 743 decreasing margin D values at finer scales for such intervals down to $r = 10$ m and measured
 744 $D \geq 1.20$ only at scales of $r \geq 31.6$ m. Wroblewski et al. (2019) also measured $D \sim 1.28$ at $r^* =$
 745 152 m for a dacite lobe that entered the ocean, though Pyle & Elliott (2006) measured $D = 1.05$
 746 for $r^* = 10$ m for another lobe from the same eruption that was emplaced subaerially. For the
 747 non-mafic IDA-01 in the present study, we measure $D \leq 1.09$ (rounded to the nearest hundredth)
 748 across meter scales.

749 However, the margin of rubbly and slabby IDA-02 has $D \geq 1.20$ for $r^* \geq 11.4$ m, and
 750 no meter-scale result of Bruno et al. (1994) has $r^* > 4$ m, so some caution is advised at high
 751 meter scales. Moreover, note that Bray et al. (2018) reported margin D values of ~ 1.30 – 1.35 for
 752 three lunar granular flows using the divider method (section 3.2.2) at decameter scales, and we
 753 measure margin D values in that same range at $r^* \geq 5.8$ m for HAW-09, a pāhoehoe margin.

754 5.3.3 Intermediate margin D

755 Among best-suited margin intervals on shallow slopes (generally $\lesssim 4^\circ$) in the present
 756 study, all four interval from transitional lava types have D values in the range 1.10–1.12 at some
 757 scale in $r^* = 1\text{--}10$ m, but no interval from another morphologic type has a D value in that range.
 758 For Bruno et al. (1994), and again considering only best-suited margin intervals on shallow
 759 slopes analyzed at meter scales, two of the four interval from transitional lava types have D
 760 values in the same 1.10–1.12 range, and only one mafic interval of any other morphologic type,
 761 pāhoehoe, has a D value in this range. The other 21 pāhoehoe margin intervals in that study have
 762 $D \geq 1.14$. (For completeness, we note that Bruno et al. (1994) did not specify by what criteria
 763 they determined a slope to qualify as shallow.)

764 We propose that for best-suited basaltic lava margins on shallow slopes, meter-scale D
 765 values of 1.10–1.12 (rounded to the nearest hundredth) are most commonly associated with
 766 transitional morphologic types (cf. Bruno et al., 1994). However, the results of Bruno et al.
 767 (1994) for non-mafic lava margin intervals suggests that caution should be taken when it is not
 768 known whether a flow is mafic. Among margin intervals of basaltic andesite, they measured D
 769 values of 1.10 and 1.13 for two of four intervals using r of 10–31.6 m and observed a trend of
 770 decreasing D values with fining scale for r of 10–4500 m. These observations suggest that non-
 771 mafic margin intervals may also be associated with meter-scale D values of 1.10–1.12, though
 772 the one example of a non-mafic margin interval from the present study, IDA-01, has lower D
 773 values (section 5.1.2). Likewise, the results in the present study for HAW-15, on a 15° slope
 774 (section 5.1.3), suggest that morphologic types with higher intrinsic meter-scale margin D values
 775 could have those values depressed into the range 1.10–1.12 by steep slopes.

776 5.3.4 Low margin D

777 Our results suggest that both ‘a‘ā, as noted by Bruno et al. (1994), and some transitional
 778 lava types have intrinsic meter-scale margin $D \leq 1.09$, at least at some scales. The non-mafic
 779 IDA-01 in the present study also has $D \leq 1.09$ (rounded to the nearest hundredth) across all
 780 analyzed scales. Similarly, Bruno et al. (1994) reported margin $D \leq 1.09$ for all four intervals of
 781 dacite and rhyolite and for one of four intervals of basaltic andesite using r of 10–31.6 m (and, as
 782 noted above, observed a trend of decreasing D values with fining scale).

783 Nonetheless, relatively low meter-scale margin D values potentially support the exclusion
 784 of pāhoehoe for best-suited flows, subject to some caveats. As pāhoehoe has intrinsic meter-scale
 785 margin $D \geq 1.13$ (section 5.3.2), the measurement of a meter-scale margin $D < 1.13$ for a best-
 786 suited lava flow on a shallow slope would suggest that the margin is not pāhoehoe. Similarly, if
 787 the D values for systematically sampled best-suited margin intervals in a flow field or region are
 788 < 1.13 at meter scales, pāhoehoe would be unlikely to dominate in that location unless steep
 789 slopes are also abundant. This test is particularly valuable in view of the hypothesis of Self et al.
 790 (1998) that pāhoehoe is the typical morphologic type of large lava deposits.

791 Moreover, this statistical exclusion test may be applicable at coarser scales and possibly
 792 to other planetary surfaces. Bruno et al. (1994) measured $D \geq 1.13$ for 15 of 16 meter-scale
 793 (field) analyses of pāhoehoe margin intervals and for 7 of 7 (photographic) analyses at coarser
 794 scales. Furthermore, Bruno and Taylor (1995) analyzed margin intervals from lava flows on
 795 Venus using both margin fractal analysis and an independent classification framework based on

796 radar-derived surface roughness (Campbell & Campbell, 1992). For all 11 margin intervals with
797 $D \geq 1.13$, the radar-based framework classified each as pāhoehoe or transitional.

798 **6 Conclusions**

799 In the field, we measured the geometry of 15 geomorphically fresh lava flow margin
800 intervals with decimeter precision. These intervals come from Hawai‘i, Iceland, and Idaho and
801 represent a wide variety of morphologic types. Based on multi-scale fractal analysis of these
802 geometries, we make the following conclusions.

- 803 1. Across representative scales of ~1–10 m (i.e., meter scales), lava flow margins exhibit
804 diverse geometric behaviors. This diversity includes empirical fractality that varies from
805 strongly scale-dependent to relatively scale-independent, even among flows of the same
806 morphologic type.
- 807 2. The respective fractal behaviors of pāhoehoe margins and margins of transitional lava
808 types partially overlap at meter scales, including both effective fractal dimensions and
809 relative scale dependence. Therefore, these types cannot always be distinguished based
810 on margin fractal analysis alone at these scales.
- 811 3. Steep slopes and topographic confinement can strongly depress the effective fractal
812 dimension of lava margins. Consequently, margins of morphologic types that have
813 intrinsically low effective fractal dimensions cannot be distinguished from margins of
814 other morphologic types at meter scales unless the topographic context at the time of the
815 flow’s emplacement is independently constrained.
- 816 4. In view of these results, we propose a new interpretive framework for meter-scale fractal
817 analysis of lava flow margins. Within this framework, $D \geq 1.13$ is consistent with
818 pāhoehoe and some transitional types, and $D \geq 1.20$ strongly suggests pāhoehoe; D in
819 the range 1.10–1.12 on shallow slopes is most commonly associated with flows of
820 transitional lava types; and $D < 1.13$ on a shallow slope suggests that a margin is not
821 pāhoehoe. This framework is best suited to geomorphically fresh flows that were
822 emplaced subaerially on Earth without significant topographic confinement, but may also
823 have value in other contexts.

824

825 **Acknowledgments and Data**

826 Work in Hawai‘i Volcanoes National Park and Craters of the Moon National Monument
827 and Preserve was conducted under science permits HAVO-2012-SCI-0025, HAVO-2016-SCI-
828 0047, and CRMO-2014-SCI-0004. Work at Holuhraun was conducted with permission from the
829 Vatnajökull National Park (Vatnajökulsþjóðgarður) service. This material is based in part on
830 work supported by the National Science Foundation Graduate Research Fellowship under Grant
831 No. 2012116373, the University of Western Ontario, the Natural Sciences and Engineering
832 Research Council, the Canadian Space Agency, NASA’s Solar System Exploration Research
833 Virtual Institute (SSERVI)/Field Investigations to Enable Solar System Science and Exploration
834 (FINESSE), a Geological Society of America Research Grant, and Dan Cavanagh. C.W.H.
835 acknowledges support from the NASA Planetary Science and Technology from Analog Research
836 (PSTAR) program (Grant # 80NSSC21K0011). We also thank Alfred McEwen for his valuable
837 support, an anonymous reviewer for their comments that improved this manuscript, and Trevor

838 Miller, Stephen Scheidt, Youngmin JeongAhn, Xianyu Tan, and Hester Mallonee for their
839 assistance in the field. The geometries of the 15 margin intervals and the synthetic fractals from
840 Figure 2 are archived in this in-text reference: (Schaefer, 2020a). The Python code used to
841 perform fractal analysis is archived in this in-text reference: (Schaefer, 2020b).

842

843

844 **References**

- 845 Anderson, S. W., McColley, S. M., Fink, J. H., & Hudson, R. K. (2005). The development of
846 fluid instabilities and preferred pathways in lava flow interiors: Insights from analog
847 experiments and fractal analysis. *Geological Society of America Special Paper 396*,
848 2396(10), 147–161. <https://doi.org/10.1130/0-8137-2396-5.147>
- 849 Andrie, R. (1992). Estimating fractal dimension with the divider method in geomorphology.
850 *Geomorphology*, 5(1–2), 131–141. [https://doi.org/10.1016/0169-555X\(92\)90061-R](https://doi.org/10.1016/0169-555X(92)90061-R)
- 851 Andrie, R. (1996a). Complexity and Scale in Geomorphology: Statistical Self-Similarity vs.
852 Characteristic Scales. *Mathematical Geology*, 28(3), 275–293.
853 <https://doi.org/10.1007/BF02083201>
- 854 Andrie, R. (1996b). The west coast of Britain: Statistical self-similarity vs. characteristic scales
855 in the landscape. *Earth Surface Processes and Landforms*, 21(10), 955–962.
856 [https://doi.org/10.1002/\(SICI\)1096-9837\(199610\)21:10<955::AID-ESP639>3.0.CO;2-Y](https://doi.org/10.1002/(SICI)1096-9837(199610)21:10<955::AID-ESP639>3.0.CO;2-Y)
- 857 Avnir, D., Biham, O., Lidar, D., & Malcai, O. (1998). Is the Geometry of Nature Fractal?
858 *Science (New York, N.Y.)*, 279(5347), 39–40.
- 859 Blake, S., & Bruno, B. . (2000). Modelling the emplacement of compound lava flows. *Earth and*
860 *Planetary Science Letters*, 184(1), 181–197. [https://doi.org/10.1016/S0012-821X\(00\)00278-](https://doi.org/10.1016/S0012-821X(00)00278-8)
861 8
- 862 Bonnefoy, L. E., Hamilton, C. W., Scheidt, S. P., Duhamel, S., Höskuldsson, Jónsdóttir, I., et al.
863 (2019). Landscape evolution associated with the 2014–2015 Holuhraun eruption in Iceland.
864 *Journal of Volcanology and Geothermal Research*, 387, 106652.
865 <https://doi.org/10.1016/j.jvolgeores.2019.07.019>
- 866 Bray, V. J., Atwood-Stone, C., Neish, C. D., Artemieva, N. A., McEwen, A. S., & McElwaine, J.
867 N. (2018). Lobate impact melt flows within the extended ejecta blanket of Pierazzo crater.
868 *Icarus*, 301, 26–36. <https://doi.org/10.1016/J.ICARUS.2017.10.002>
- 869 Bruno, B. C., & Taylor, G. J. (1995). Morphologic identification of Venusian lavas. *Geophysical*
870 *Research Letters*, 22(14), 1897–1900. <https://doi.org/10.1029/95GL01318>
- 871 Bruno, B. C., Taylor, G. J., Rowland, S. K., Lucey, P. G., & Self, S. (1992). Lava Flows are
872 Fractals. *Geophysical Research Letters*, 19(3), 305–308. <https://doi.org/10.1029/91gl03039>
- 873 Bruno, B. C., Taylor, G. J., Rowland, S. K., & Baloga, S. M. (1994). Quantifying the effect of
874 rheology on lava-flow margins using fractal geometry. *Bulletin of Volcanology*, 56(3), 193–
875 206. <https://doi.org/10.1007/BF00279604>
- 876 Campbell, B. A., & Campbell, D. B. (1992). Analysis of volcanic surface-morphology on Venus
877 from comparison of Arecibo, Magellan, and terrestrial airborne radar data. *Journal of*
878 *Geophysical Research-Planets*, 97(E10), 16293–16314. <https://doi.org/10.1029/92JE01558>

- 879 Cashman, K. V., Thornber, C., & Kauahikaua, J. P. (1999). Cooling and crystallization of lava in
 880 open channels, and the transition of Pāhoehoe Lava to 'A'ā. *Bulletin of Volcanology*, 61(5),
 881 306–323. <https://doi.org/10.1007/s004450050299>
- 882 Chowdhury, A. R., Saxena, M., Kumar, A., Joshi, S. R., Amitabh, Dagar, A., et al. (2020).
 883 Orbiter high resolution camera onboard chandrayaan-2 orbiter. *Current Science*, 118(4),
 884 560–565. <https://doi.org/10.18520/cs/v118/i4/560-565>
- 885 Christensen, P. R., Jakosky, B. M., Kieffer, H. H., Malin, M. C., McSween, H. Y., Neelson, K.,
 886 et al. (2004). The Thermal Emission Imaging System (THEMIS) for the Mars 2001
 887 Odyssey mission. *Space Science Reviews*. Springer.
 888 <https://doi.org/10.1023/b:spac.0000021008.16305.94>
- 889 Christensen, P. R., McSween, H. Y., Bandfield, J. L., Ruff, S. W., Rogers, A. D., Hamilton, V.
 890 E., et al. (2005). Evidence for magmatic evolution and diversity on Mars from infrared
 891 observations. *Nature*, 436(7050), 504–509. <https://doi.org/10.1038/nature03639>
- 892 Economou, T. (2001). Chemical analyses of martian soil and rocks obtained by the Pathfinder
 893 Alpha Proton X-ray spectrometer. In *Radiation Physics and Chemistry* (Vol. 61, pp. 191–
 894 197). Pergamon. [https://doi.org/10.1016/S0969-806X\(01\)00240-7](https://doi.org/10.1016/S0969-806X(01)00240-7)
- 895 Evangelidis, G. D., & Psarakis, E. Z. (2008). Parametric image alignment using enhanced
 896 correlation coefficient maximization. *IEEE Transactions on Pattern Analysis and Machine*
 897 *Intelligence*, 30(10), 1858–1865. <https://doi.org/10.1109/TPAMI.2008.113>
- 898 Falconer, K. (2003). *Fractal Geometry: Mathematical Foundations and Applications, Second*
 899 *Edition*. Wiley & Sons. <https://doi.org/10.1002/0470013850>
- 900 Finch, R. H. (1933). Block Lava. *The Journal of Geology*, 41(7), 769–770.
 901 <https://doi.org/10.1086/624096>
- 902 Gaonac'h, H., Lovejoy, S., & Stix, J. (1992). Scale invariance of basaltic lava flows and their
 903 fractal dimensions. *Geophysical Research Letters*, 19(8), 785–788.
 904 <https://doi.org/10.1029/92GL00545>
- 905 Gneiting, T., & Schlather, M. (2004). Stochastic models that separate fractal dimension and the
 906 hurst effect. *SIAM Review*, 46(2), 269–282. <https://doi.org/10.1137/S0036144501394387>
- 907 Gneiting, T., Ševčíková, H., & Percival, D. B. (2012). Estimators of fractal dimension: Assessing
 908 the roughness of time series and spatial data. *Statistical Science*, 27(2), 247–277.
 909 <https://doi.org/10.1214/11-STS370>
- 910 Gregg, T. K. P. (2017). Patterns and processes: Subaerial lava flow morphologies: A review.
 911 *Journal of Volcanology and Geothermal Research*, 342, 3–12.
 912 <https://doi.org/10.1016/J.JVOLGEORES.2017.04.022>
- 913 Hamilton, C. W. (2019). “Fill and spill” lava flow emplacement: Implications for understanding
 914 planetary flood basalt eruptions. In N. F. Six & G. Karr (Eds.), *Marshall Space Flight*

- 915 *Center Faculty Fellowship Program* (p. 9). NASA (TM—2019–220139). Retrieved from
 916 <https://ntrs.nasa.gov/archive/nasa/casi.ntrs.nasa.gov/20200000048.pdf>
- 917 Hamilton, C. W., Scheidt, S. P., Sori, M. M., Wet, A. P., Bleacher, J. E., Mougini-Mark, P. J., et
 918 al. (2020). Lava-Rise Plateaus and Inflation Pits in the McCartys Lava Flow Field, New
 919 Mexico: An Analog for Pāhoehoe-Like Lava Flows on Planetary Surfaces. *Journal of*
 920 *Geophysical Research: Planets*, 125(7). <https://doi.org/10.1029/2019JE005975>
- 921 Harris, A. J. L., Rowland, S. K., Villeneuve, N., & Thordarson, T. (2017). Pāhoehoe, ‘a‘ā, and
 922 block lava: an illustrated history of the nomenclature. *Bulletin of Volcanology*, 79(1), 7.
 923 <https://doi.org/10.1007/s00445-016-1075-7>
- 924 Hayward, J., Orford, J. D., & Brian Whalley, W. (1989). Three implementations of fractal
 925 analysis of particle outlines. *Computers and Geosciences*, 15(2), 199–207.
 926 [https://doi.org/10.1016/0098-3004\(89\)90034-4](https://doi.org/10.1016/0098-3004(89)90034-4)
- 927 Holcomb, R. T. (1987). Eruptive history and long-term behavior of Kilauea Volcano. In R. W.
 928 Decker, T. L. Wright, & P. H. Stauffer (Eds.), *Volcanism in Hawaii: U.S. Geological*
 929 *Survey Professional Paper 1350, Volume 1* (pp. 261–350).
- 930 Hon, K., Gansecki, C., & Kauahikaua, J. (2003). The Transition from ‘A‘ā to Pāhoehoe Crust on
 931 Flows Emplaced During the Pu‘u ‘Ō‘ō-Kūpaianaha Eruption. *USGS Prof. Paper 1676*, 89–
 932 103. [https://doi.org/10.1016/0003-6870\(73\)90259-7](https://doi.org/10.1016/0003-6870(73)90259-7)
- 933 Hughes, S. S., Haberle, C. W., Kobs Nawotniak, S. E., Sehlke, A., Garry, W. B., Elphic, R. C., et
 934 al. (2019). Basaltic Terrains in Idaho and Hawai‘i as Planetary Analogs for Mars Geology
 935 and Astrobiology. *Astrobiology*, 19(3), 260–283. <https://doi.org/10.1089/ast.2018.1847>
- 936 Keszthelyi, L. P. (2002). Classification of the mafic lava flows from ODP Leg 183. *Proceedings*
 937 *of the Ocean Drilling Program, Scientific Results*, 183(February), 1–28.
- 938 Keszthelyi, L. P., McEwen, A. S., & Thordarson, T. (2000). Terrestrial analogs and thermal
 939 models for Martian flood lavas. *Journal of Geophysical Research: Planets*, 105(E6),
 940 15027–15049. <https://doi.org/10.1029/1999JE001191>
- 941 Keszthelyi, L. P., Thordarson, T., McEwen, A., Haack, H., Guilbaud, M. N., Self, S., & Rossi,
 942 M. J. (2004). Icelandic analogs to Martian flood lavas. *Geochemistry, Geophysics,*
 943 *Geosystems*, 5(11), Q11014. <https://doi.org/10.1029/2004GC000758>
- 944 Kilburn, C. R. J. (1990). Surfaces of Aa Flow-Fields on Mount Etna, Sicily: Morphology,
 945 Rheology, Crystallization and Scaling Phenomena. In J. H. Fink (Ed.), *Lava Flows and*
 946 *Domes: Emplacement Mechanisms and Hazard Implications* (pp. 129–156). Berlin
 947 Heidelberg: Springer-Verlag. https://doi.org/10.1007/978-3-642-74379-5_6
- 948 Kilburn, C. R. J. (1996). Patterns and predictability in the emplacement of subaerial lava flows
 949 and flow fields. In *Monitoring and Mitigation of Volcano Hazards* (pp. 491–537). Berlin
 950 Heidelberg: Springer-Verlag. https://doi.org/doi:10.1007%2F978-3-642-80087-0_15

- 951 Kirk, R. L., Howington-Kraus, E., Rosiek, M. R., Anderson, J. A., Archinal, B. A., Becker, K. J.,
 952 et al. (2008). Ultrahigh resolution topographic mapping of Mars with MRO HiRISE stereo
 953 images: Meter-scale slopes of candidate Phoenix landing sites. *Journal of Geophysical*
 954 *Research*, 113, E00A24. <https://doi.org/10.1029/2007JE003000>
- 955 Klinkenberg, B. (1994). A review of methods used to determine the fractal dimension of linear
 956 features. *Mathematical Geology*, 26(1), 23–46. <https://doi.org/10.1007/BF02065874>
- 957 Klinkenberg, B., & Goodchild, M. F. (1992). The fractal properties of topography: A comparison
 958 of methods. *Earth Surface Processes and Landforms*, 17(3), 217–234.
 959 <https://doi.org/10.1002/esp.3290170303>
- 960 Kolzenburg, S., Giordano, D., Thordarson, T., Höskuldsson, A., & Dingwell, D. B. (2017). The
 961 rheological evolution of the 2014/2015 eruption at Holuhraun, central Iceland. *Bulletin of*
 962 *Volcanology*, 79(6), 45. <https://doi.org/10.1007/s00445-017-1128-6>
- 963 Kuntz, M. A., Champion, D. E., Spiker, E. C., Lefebvre, R. H., & Mcbroomes, L. A. (1982).
 964 The Great Rift and the Evolution of the Craters of the Moon Lava Field, Idaho. *Cenozoic*
 965 *Geology of Idaho: Idaho Bureau of Mines and Geology Bulletin*, 26, 423–437. Retrieved
 966 from http://geology.isu.edu/Digital_Geology_Idaho/papers/B-26ch7-2.pdf
- 967 Kuntz, M. A., Elsheimer, H. N., Espos, L. F., & Klock, P. R. (1985). *USGS Open-File Report*
 968 *85-0593: Major-element analyses of latest Pleistocene-Holocene lava fields of the Snake*
 969 *River plain, Idaho*. Retrieved from
 970 [http://search.ebscohost.com/login.aspx?direct=true&db=geh&AN=1986-](http://search.ebscohost.com/login.aspx?direct=true&db=geh&AN=1986-014534&site=ehost-live)
 971 [014534&site=ehost-live](http://search.ebscohost.com/login.aspx?direct=true&db=geh&AN=1986-014534&site=ehost-live)
- 972 Kuntz, M. A., Spiker, E. C., Rubin, M., Champion, D. E., & Lefebvre, R. H. (1986).
 973 Radiocarbon studies of latest Pleistocene and Holocene lava flows of the Snake River Plain,
 974 Idaho: Data, lessons, interpretations. *Quaternary Research*, 25(2), 163–176.
 975 [https://doi.org/10.1016/0033-5894\(86\)90054-2](https://doi.org/10.1016/0033-5894(86)90054-2)
- 976 Kvålseth, T. O. (1985). Cautionary Note about R^2 . *American Statistician*, 39(4), 279–285.
 977 <https://doi.org/10.1080/00031305.1985.10479448>
- 978 Leeman, W. P., Vitaliano, C. J., & Prinz, M. (1976). Evolved Lavas from the Snake River Plain.
 979 *Contributions to Mineralogy and Petrology*, 56, 35–60. Retrieved from [https://link-](https://link-springer-com.ezproxy1.library.arizona.edu/content/pdf/10.1007%2FBF00375420.pdf)
 980 [springer-com.ezproxy1.library.arizona.edu/content/pdf/10.1007%2FBF00375420.pdf](https://link-springer-com.ezproxy1.library.arizona.edu/content/pdf/10.1007%2FBF00375420.pdf)
- 981 Li, M., & Li, J. Y. (2017). Generalized Cauchy model of sea level fluctuations with long-range
 982 dependence. *Physica A: Statistical Mechanics and Its Applications*, 484, 309–335.
 983 <https://doi.org/10.1016/j.physa.2017.04.130>
- 984 Lipman, P. W., & Banks, N. G. (1987). Aa flow dynamics, Mauna Loa 1984. In R. W. Decker,
 985 T. L. Wright, & P. H. Stauffer (Eds.), *Volcanism in Hawaii: U.S. Geological Survey*
 986 *Professional Paper 1350, Volume 2* (pp. 1527–1567). Retrieved from
 987 <https://www.researchgate.net/publication/262261672>

- 988 Luongo, G., Mazzarella, A., & Di Donna, G. (2000). Multifractal characterization of Vesuvio
 989 lava-flow margins and its implications. *Journal of Volcanology and Geothermal Research*,
 990 *101*(3–4), 307–311. [https://doi.org/10.1016/S0377-0273\(00\)00175-X](https://doi.org/10.1016/S0377-0273(00)00175-X)
- 991 Macdonald, G. A. (1953). Pahoehoe, aa, and block lava. *American Journal of Science*, *251*(3),
 992 169–191. <https://doi.org/10.2475/ajs.251.3.169>
- 993 Maeno, F., Nakada, S., & Kaneko, T. (2016). Morphological evolution of a new volcanic islet
 994 sustained by compound lava flows. *Geology*, *44*(4), 259–262.
 995 <https://doi.org/10.1130/G37461.1>
- 996 Mandelbrot, B. B. (1967). How Long Is the Coast of Britain? Statistical Self-similarity and
 997 Fractional Dimension. *Science (New York, N.Y.)*, *156*(3775), 636–638.
 998 <https://doi.org/10.1126/science.156.3775.636>
- 999 Mandelbrot, B. B. (1982). *The Fractal Geometry of Nature*. New York: W.H. Freeman.
 1000 <https://doi.org/10.2307/3615422>
- 1001 Mandelbrot, B. B. (1986). Self-affine fractal sets, II: Length and surface dimensions. In *Fractals*
 1002 *in Physics* (pp. 17–20). Elsevier. <https://doi.org/10.1016/b978-0-444-86995-1.50005-6>
- 1003 Mandelbrot, B. B. (2002). *Gaussian Self-Affinity and Fractals: Globality, the Earth, 1/f Noise,*
 1004 *and R/S*. New York: Springer-Verlag.
- 1005 Maria, A., & Carey, S. (2002). Using fractal analysis to quantitatively characterize the shapes of
 1006 volcanic particles. *Journal of Geophysical Research: Solid Earth*, *107*(B11), ECV 7-1-ECV
 1007 7-17. <https://doi.org/10.1029/2001jb000822>
- 1008 Mark, D. M., & Aronson, P. B. (1984). Scale-dependent fractal dimensions of topographic
 1009 surfaces: An empirical investigation, with applications in geomorphology and computer
 1010 mapping. *Journal of the International Association for Mathematical Geology*, *16*(7), 671–
 1011 683. <https://doi.org/10.1007/BF01033029>
- 1012 McEwen, A. S., Eliason, E. M., Bergstrom, J. W., Bridges, N. T., Hansen, C. J., Delamere, W.
 1013 A., et al. (2007). Mars Reconnaissance Orbiter’s High Resolution Imaging Science
 1014 Experiment (HiRISE). *Journal of Geophysical Research*, *112*, E05S02.
 1015 <https://doi.org/10.1029/2005JE002605>
- 1016 Mitchell, N. C., Beier, C., Rosin, P. L., Quartau, R., & Tempera, F. (2008). Lava penetrating
 1017 water: Submarine lava flows around the coasts of Pico Island, Azores. *Geochemistry,*
 1018 *Geophysics, Geosystems*, *9*(3), n/a-n/a. <https://doi.org/10.1029/2007GC001725>
- 1019 Moratto, Z., Nefian, A., Beyer, R., Hancher, M., Lundy, M., ALEXANDROV, O., et al. (2013).
 1020 Ames Stereo Pipeline, NASA’s Open Source Automated Stereogrammetry Software. *Lunar*
 1021 *and Planetary Science Conference*, 2364. Retrieved from
 1022 <https://www.lpi.usra.edu/meetings/lpsc2010/pdf/2364.pdf>
- 1023 Moré, J. J. (1978). The Levenberg-Marquardt algorithm: Implementation and theory. In G. A.

- 1024 Watson (Ed.), *Numerical Analysis* (pp. 105–116). Springer-Verlag.
1025 <https://doi.org/10.1007/BFb0067700>
- 1026 Neish, C. D., Hamilton, C. W., Hughes, S. S., Nawotniak, S. K., Garry, W. B., Skok, J. R., et al.
1027 (2017). Terrestrial analogues for lunar impact melt flows. *Icarus*, *281*, 73–89.
1028 <https://doi.org/10.1016/j.icarus.2016.08.008>
- 1029 Neuman, S. P., Guadagnini, A., Riva, M., & Siena, M. (2013). Recent Advances in Statistical
1030 and Scaling Analysis of Earth and Environmental Variables. In *Advances in Hydrogeology*
1031 (pp. 1–25). New York, NY: Springer New York. [https://doi.org/10.1007/978-1-4614-6479-](https://doi.org/10.1007/978-1-4614-6479-2_1)
1032 [2_1](https://doi.org/10.1007/978-1-4614-6479-2_1)
- 1033 Pedersen, G. B. M., Höskuldsson, A., Dürig, T., Thordarson, T., Jónsdóttir, I., Riishuus, M. S., et
1034 al. (2017). Lava field evolution and emplacement dynamics of the 2014–2015 basaltic
1035 fissure eruption at Holuhraun, Iceland. *Journal of Volcanology and Geothermal Research*,
1036 *340*, 155–169. <https://doi.org/10.1016/J.JVOLGEORES.2017.02.027>
- 1037 Peterson, D. W., & Tilling, R. I. (1980). Transition of basaltic lava from pahoehoe to aa, Kilauea
1038 Volcano, Hawaii: Field observations and key factors. *Journal of Volcanology and*
1039 *Geothermal Research*, *7*(3–4), 271–293. [https://doi.org/10.1016/0377-0273\(80\)90033-5](https://doi.org/10.1016/0377-0273(80)90033-5)
- 1040 Pyle, D. M., & Elliott, J. R. (2006). Quantitative morphology, recent evolution, and future
1041 activity of the Kamani Islands volcano, Santorini, Greece. *Geosphere*, *2*(5), 253.
1042 <https://doi.org/10.1130/GES00028.1>
- 1043 Richardson, L. F. (1961). The problem of contiguity: An appendix to “Statistic of Deadly
1044 Quarrels.” *General Systems: Yearbook of the Society for the Advancement of General*
1045 *Systems Theory*, *6*, 139–187. Retrieved from <http://cds.cern.ch/record/434833>
- 1046 Rieder, R., Economou, T., Wänke, H., Turkevich, A., Crisp, J., Brückner, J., et al. (1997,
1047 December 5). The chemical composition of martian soil and rocks returned by the mobile
1048 alpha proton x-ray spectrometer: Preliminary results from the x-ray mode. *Science*.
1049 American Association for the Advancement of Science.
1050 <https://doi.org/10.1126/science.278.5344.1771>
- 1051 Robinson, M. S., Brylow, S. M., Tschimmel, M., Humm, D., Lawrence, S. J., Thomas, P. C., et
1052 al. (2010). Lunar Reconnaissance Orbiter Camera (LROC) Instrument Overview. *Space*
1053 *Science Reviews*, *150*(1–4), 81–124. <https://doi.org/10.1007/s11214-010-9634-2>
- 1054 Rowland, S. K., & Walker, G. P. (1990). Pahoehoe and aa in Hawaii: volumetric flow rate
1055 controls the lava structure. *Bulletin of Volcanology*, *52*(8), 615–628.
1056 <https://doi.org/10.1007/BF00301212>
- 1057 Rowland, S. K., & Walker, G. P. L. (1987). Toothpaste lava: Characteristics and origin of a lava
1058 structural type transitional between pahoehoe and aa. *Bulletin of Volcanology*, *49*(4), 631–
1059 641. <https://doi.org/10.1007/BF01079968>
- 1060 Sandmeyer, E., Nawotniak, S. E. K., Hughes, S. S., Elphic, R. C., Lim, D. S. S., & Heldmann, J.

- 1061 (2017). Frothy Lava At Highway Flow, Craters of the Moon. *Lunar and Planetary Science*
1062 *Conference*, #2838. Retrieved from
1063 <https://www.hou.usra.edu/meetings/lpsc2017/pdf/2838.pdf>
- 1064 Schaefer, E. I. (2020a). Geometries of fresh lava margins and some relevant synthetic fractals.
1065 Retrieved February 17, 2021, from <https://doi.pangaea.de/10.1594/PANGAEA.925792>
- 1066 Schaefer, E. I. (2020b). Scale-dependent Fractal Analysis (ver. 0.1).
1067 <https://doi.org/10.17504/protocols.io.bmm2k48e>
- 1068 Self, S., Thordarson, T., Keszthelyi, L. P., Walker, G. P. L., Hon, K., Murphy, M. T., et al.
1069 (1996). A new model for the emplacement of Columbia River basalts as large, inflated
1070 Pahoehoe Lava Flow Fields. *Geophysical Research Letters*, 23(19), 2689–2692.
1071 <https://doi.org/10.1029/96GL02450>
- 1072 Self, S., Keszthelyi, L. P., & Thordarson, T. (1998). The Importance of Pāhoehoe. *Annu. Rev.*
1073 *Earth Planet. Sci.*, 26, 81–110. <https://doi.org/10.1146/annurev.earth.26.1.81>
- 1074 Shean, D. E., Alexandrov, O., Moratto, Z. M., Smith, B. E., Joughin, I. R., Porter, C., & Morin,
1075 P. (2016). An automated, open-source pipeline for mass production of digital elevation
1076 models (DEMs) from very-high-resolution commercial stereo satellite imagery. *ISPRS*
1077 *Journal of Photogrammetry and Remote Sensing*, 116, 101–117.
1078 <https://doi.org/10.1016/j.isprsjprs.2016.03.012>
- 1079 Shenker, O. R. (1994). Fractal geometry is not the geometry of nature. *Studies in History and*
1080 *Philosophy of Science Part A*, 25(6), 967–981. [https://doi.org/10.1016/0039-](https://doi.org/10.1016/0039-3681(94)90072-8)
1081 [3681\(94\)90072-8](https://doi.org/10.1016/0039-3681(94)90072-8)
- 1082 Shepard, M. K., Brackett, R. A., & Arvidson, R. E. (1995). Self-affine (fractal) topography:
1083 Surface parameterization and radar scattering. *Journal of Geophysical Research*, 100(E6),
1084 11709. <https://doi.org/10.1029/95JE00664>
- 1085 Shepard, M. K., Campbell, B. A., Bulmer, M. H., Farr, T. G., Gaddis, L. R., & Plaut, J. J. (2001).
1086 The roughness of natural terrain: a planetary and remote sensing perspective. *Journal of*
1087 *Geophysical Research*, 106(E12), 32777–32795. <https://doi.org/10.1029/2000JE001429>
- 1088 Soule, S. A., & Cashman, K. V. (2005). Shear rate dependence of the pāhoehoe-to-‘a‘ā
1089 transition: Analog experiments. *Geology*, 33(5), 361. <https://doi.org/10.1130/G21269.1>
- 1090 Stout, M. Z., Nicholls, J., & Kuntz, M. A. (1994). Petrological and mineralogical variations in
1091 2500-2000 yr B.P. Lava Flows, craters of the moon lava field, idaho. *Journal of Petrology*,
1092 35(6), 1681–1715. <https://doi.org/10.1093/petrology/35.6.1681>
- 1093 Thordarson, T. (1995). *Volatile release and atmospheric effects of basaltic fissure eruptions*.
1094 University of Hawaii, Manoa.
- 1095 Thordarson, T., & Höskuldsson, Á. (2008). Postglacial volcanism in Iceland. *Jökull*, 58, 197–
1096 228.

- 1097 Tolometti, G. D., Neish, C. D., Osinski, G. R., Hughes, S. S., & Nawotniak, S. E. K. (2020).
1098 Interpretations of lava flow properties from radar remote sensing data. *Planetary and Space*
1099 *Science*, 190, 104991. <https://doi.org/10.1016/j.pss.2020.104991>
- 1100 Voigt, J. R. C., & Hamilton, C. W. (2018). Investigating the volcanic versus aqueous origin of
1101 the surficial deposits in Eastern Elysium Planitia, Mars. *Icarus*, 309, 389–410.
1102 <https://doi.org/10.1016/J.ICARUS.2018.03.009>
- 1103 Voigt, J. R. C., Hamilton, C. W., Scheidt, S. P., Steinbrügge, G., Münzer, U., Höskuldsson, Á., et
1104 al. (2017). Facies Characterization of the 2014–2015 Holuhraun Lava Flow Field from
1105 Remote Sensing Data and Field Observations. *American Geophysical Union Fall Meeting*,
1106 P31H-3796. Retrieved from
1107 <https://ui.adsabs.harvard.edu/abs/2018AGUFM.P31H3796V/abstract>
- 1108 Whelley, P. L., Richardson, J. A., & Hamilton, C. W. (2017). Lava Channel Textures in Tartarus
1109 Colles, Elysium Planitia, Mars. *48th Lunar and Planetary Science Conference, Held 20-24*
1110 *March 2017, at The Woodlands, Texas. LPI Contribution No. 1964, Id.2491, 48*. Retrieved
1111 from <http://adsabs.harvard.edu/abs/2017LPI...48.2491W>
- 1112 Wilson, L., & Head, J. W. (1994). Review and analysis of volcanic eruption to theory
1113 relationships landforms. *Reviews of Geophysics*, 32(3), 221–263.
1114 <https://doi.org/10.1029/94RG01113>
- 1115 Wolfe, E. W., Neal, C. A., Banks, N. G., & Duggan, T. J. (1988). Geologic observations and
1116 chronology of eruptive events. In E. W. Wolfe (Ed.), *The Puu Oo Eruption of Kilauea*
1117 *Volcano, Hawaii; Episodes 1 Through 20, January 3, 1983, Through June 8, 1984. USGS*
1118 *Professional Paper 1463* (pp. 1–99).
- 1119 Wroblewski, F. B., Treiman, A. H., Bhiravarasu, S., & Gregg, T. K. P. (2019). Ovda Fluctus, the
1120 Festoon Lava Flow on Ovda Regio, Venus: Not Silica-Rich. *Journal of Geophysical*
1121 *Research: Planets*, 124(8), 2233–2245. <https://doi.org/10.1029/2019JE006039>
- 1122 You, J., Kauhanen, K., & Raitala, J. (1996). Fractal properties of outflows from Venusian impact
1123 craters. *Earth, Moon and Planets*, 73(3), 195–214. <https://doi.org/10.1007/BF00115880>

1124

Supporting Information for

Reexamining the potential to classify lava flows from the fractality of their margins

E. I. Schaefer^{1,2}, C. W. Hamilton³, C. D. Neish^{1,2}, M. M. Sori⁴, A. M. Bramson⁴, and S. P. Beard⁵

¹ Department of Earth Sciences, University of Western Ontario, 1151 Richmond Street N., London, Ontario, N6A 5B7 Canada

² Institute for Earth and Space Exploration, University of Western Ontario, 1151 Richmond Street N., London, Ontario, N6A 5B7 Canada

³ Lunar and Planetary Laboratory, University of Arizona, 1629 E. University Blvd., Tucson, Arizona, 85721 USA

⁴ Department of Earth, Atmospheric, and Planetary Sciences, Purdue University, 550 Stadium Mall Dr., West Lafayette, IN 47907 USA

⁵ State Key Laboratory in Lunar and Planetary Science, Macau University of Science and Technology, Avenida Wai Long, Taipa, 999078, Macau

Contents of this file

Text S1
Figures S1 to S3
Table S1

Introduction

The Supporting Information includes a text section, three figures, and a table. Two figures are provided to clarify points—one geometric and the other interpretive—from the main paper. The text section, with an accompanying figure, describes analyses used to estimate the measurement error. The table reports the results of those analyses.

Text S1.

In the main paper, we estimate that the measurement error for all 15 margin intervals is ~ 15 cm and attribute that error primarily to unintended tilt of the rover mast. For reference, a tilt of $\sim 4^\circ$ would apply an offset of 15 cm. In this section, we quantitatively assess that estimate.

For a subset of the ICE-01a margin interval, two rover operators—authors EIS and CDN—each collected vertices independently (Fig. S3). This subset has a straight-line span of 324 m, and the respective along-margin lengths of the two traces are 555 m for EIS and 509 m for CDN. In general, EIS walked the margin more slowly than CDN, which allowed him to walk more closely to the margin and collect finer spatial details than CDN (Fig. S3c). On the other hand, because of her quicker pace, CDN collected most of ICE-01a's length. In the judgement of EIS, these two operators reasonably represent most of the range of inter-operator variability among all operators in the present study.

We take 28 partially overlapping subintervals along the EIS trace, each starting a distance of 15 m along-margin from the previous subinterval. We require each subinterval to have a minimum of 1000 vertices and an along-margin length of at least 150 m. For each such subinterval from the EIS trace, we identify the corresponding subinterval from the CDN trace by proximity. The statistics for both EIS and CDN subintervals are reported in Table S1.

By comparing each CDN subinterval to its EIS counterpart, we can measure directly the precision with which repeated field collection would describe the same margin. This repeatability precision is not identical to measurement error, if that error is interpreted as the discrepancy between the field-collected vertices and the true margin. Nonetheless, we believe an estimate of repeatability precision provides a reasonable estimate of measurement error for our purposes, especially as the trace of the true margin is not independently known. Moreover, EIS generally captured as much spatial detail as any operator, so the EIS trace represents our best estimate of the true margin.

To estimate repeatability precision, we measure the distance from each vertex of each CDN subinterval to the corresponding EIS subinterval. Although only vertices represent the collected data, the fractal analysis method that we use requires interpolation between vertices. Therefore, we include the line segments between vertices as part of the EIS subintervals when calculating distance. Statistics for these distances are reported in Table S1.

A component of these distances is due to translation. As translation has no effect on fractal analysis, it is appropriate to minimize this component and recalculate distances as a better estimate of the relevant measurement error. To minimize systematic offset, we first convert each pair of EIS and CDN subintervals to binary images in which the flow and the area outside the flow are each arbitrarily colored white or black, with a pixel

scale equal to half the median inter-vertex length of that subinterval with the smaller such median. We then use Enhanced Correlation Coefficient Maximization (Evangelidis & Psarakis, 2008) to shift the CDN binary image until its correlation with the EIS binary image is maximized and apply the identified shift to the CDN subinterval to generate CDN' (Fig. S3c). The distances between CDN' vertices and EIS subintervals are reported in Table S1.

Most of the translational offset between the EIS and CDN traces is due to the fact that CDN generally maintained a wider berth from the margin than EIS (Fig. S3c). Although this offset is purely translational when individual vertices are considered, the effect at coarser scales is a rescaling. For example, when CDN walked along the perimeter of a lobe, the wider berth would expand the width of that lobe relative to the EIS trace (left side of Fig. S3c). Therefore, the translational component is more dominant at finer scales and is less effectively removed by correlation maximization at the scale of a subinterval, as we have done. The error remaining for CDN' vertices thus overestimates the error at finer scales, or equivalently, at rod lengths finer than the straight-line span of the subinterval. Among all subintervals, the range of spans is ~68–103 m, and therefore the errors calculated from CDN' are appropriate for $r \approx 68$ m. The paper focuses on r^* of 1–10 m, which correspond to r of 0.25–40 m. The errors calculated from CDN' therefore overestimate the error for this this range.

For each of the 28 subinterval pairs, we calculated the mean and median distances between CDN' vertices and the EIS trace (Table S1). The respective means for these values are 18 cm and 12 cm. We therefore conclude that the estimate of 15 cm for measurement error in the main text is reasonable.

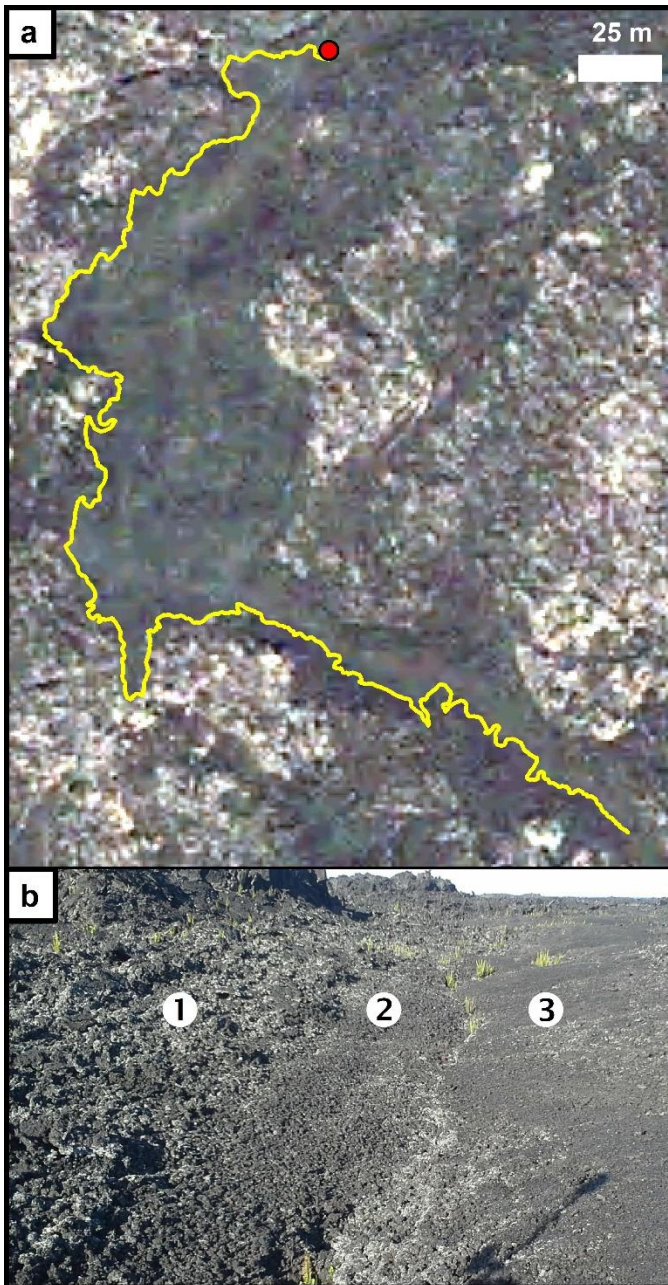


Figure S1. Primary toothpaste lava margin interval HAW-13a and context. (a) HAW-13a (yellow) on same background as Figure 1c of the main text (0.6 m/pixel). North end of HAW-13a (red dot) is location of (b). North is up. (b) Examples of (1) fragmented toothpaste slabs and rubble, (2) a spreading zone, and (3) primary toothpaste lava. View looks east and is not included in HAW-13a.

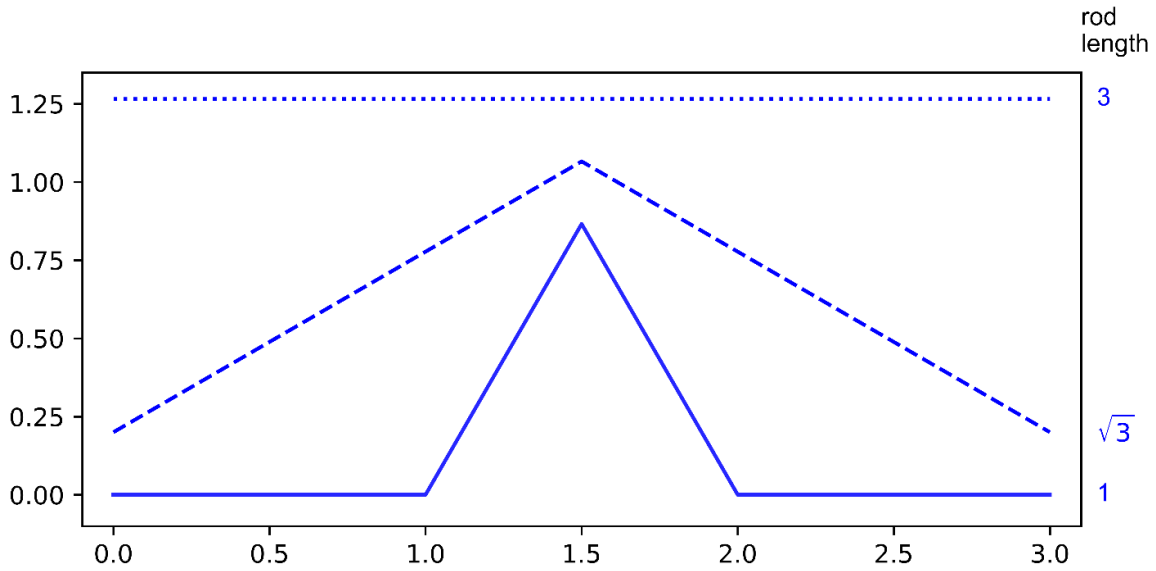


Figure S2. Rod-stepping of motif A (Figure 2a of the main text). The geometries Classic and Random (Figure 2b) are built from motif A (solid line) and its flipped counterpart motif A' (Figure 2a). The fractal scale-spectra for Classic and Random have a $\sqrt{3}$ periodicity (Figure 2c). This periodicity arises from the three modes in which motif A (and motif A') can be spanned by rods of different lengths in the divider method (section 3.2.2 of the main text). In their purest forms, the rod length of each mode (solid, dashed, and dotted lines) differs by a factor of $\sqrt{3}$.

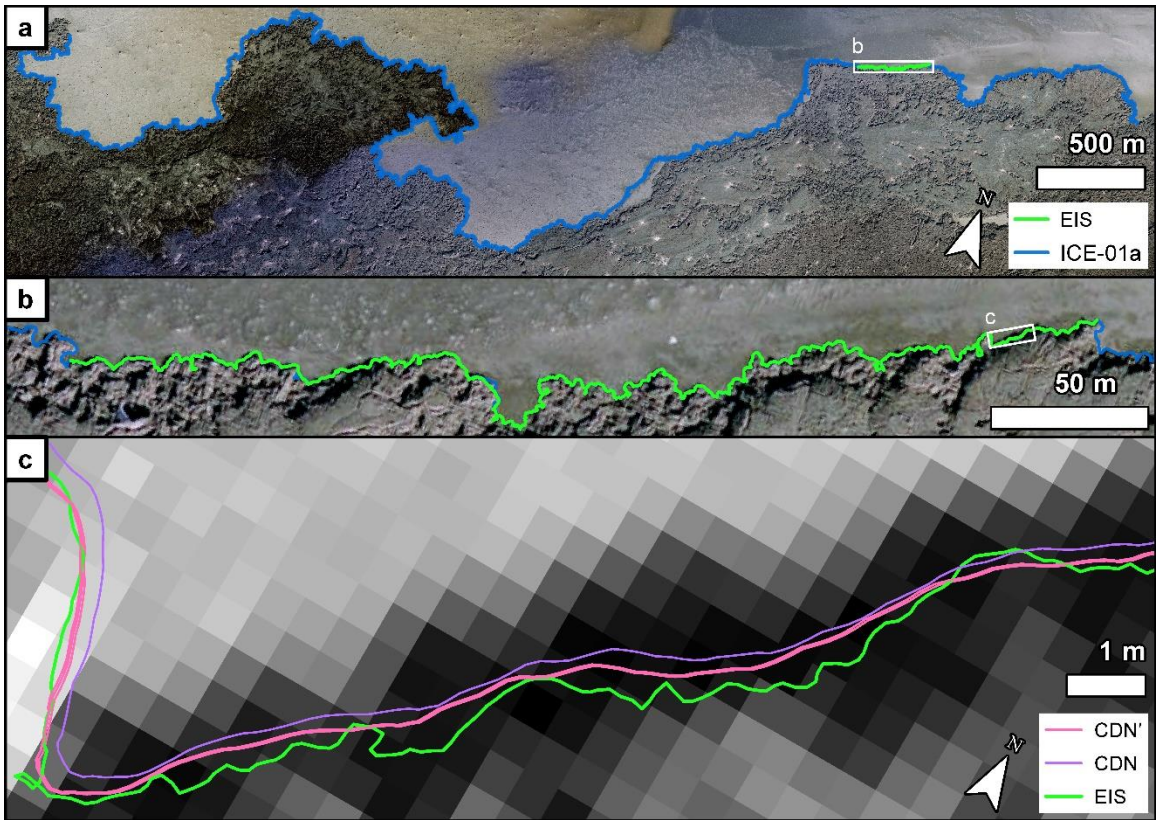


Figure S3. Repeatability precision analysis. Background in each pane is 2015 visible data from Loftmyndir ehf. (0.5 m/pixel). (a) ICE-01a is drawn in blue, and a portion of this margin interval collected by author EIS is superposed and drawn in green. (b) Magnified view of (a). (c) Magnified view of (b), but ICE-01a is not shown. Instead, counterpart intervals collected by authors EIS and CDN are drawn in green and purple, respectively. In addition, subintervals of CDN (CDN') that have been optimally translated to match counterpart EIS subintervals as nearly as possible are drawn in pink. Background is rendered in grayscale to increase color contrast with the drawn lines.

Table S1*Repeatability Precision Analysis*

Subinterval count	28	
Subinterval geometry	<u>EIS</u>	<u>CDN / CDN'</u>
Vertices per subinterval	1000–1071	824–962
Length per subinterval (m)	150–152	133–146
Straight-line span per subinterval (m)	67.9–103	67.5–103
Repeatability precision		
<u>Per-subinterval mean errors</u>	<u>vs. CDN</u>	<u>vs. CDN'</u>
Range (cm)	15–27	13–24
Mean (cm)	22	18
Standard deviation (cm)	3.5	2.5
<u>Per-subinterval median errors</u>	<u>vs. CDN</u>	<u>vs. CDN'</u>
Range (cm)	13–26	10–17
Mean (cm)	18	12
Standard deviation (cm)	4.1	1.8